HAL open science

Multiple motion encoding in Phase-Contrast MRI: A general theory and application to elastography imaging

Helge Herthum, Hugo Carrillo, Axel Osses, Sergio Uribe, Ingolf Sack, Cristobal Bertoglio

To cite this version:

Helge Herthum, Hugo Carrillo, Axel Osses, Sergio Uribe, Ingolf Sack, et al.. Multiple motion encoding in Phase-Contrast MRI: A general theory and application to elastography imaging. 2022. hal-02947225v4

HAL Id: hal-02947225

https://hal.science/hal-02947225v4

Preprint submitted on 17 Mar 2022

HAL is a multi-disciplinary open access archive for the deposit and dissemination of scientific research documents, whether they are published or not. The documents may come from teaching and research institutions in France or abroad, or from public or private research centers.

L'archive ouverte pluridisciplinaire **HAL**, est destinée au dépôt et à la diffusion de documents scientifiques de niveau recherche, publiés ou non, émanant des établissements d'enseignement et de recherche français ou étrangers, des laboratoires publics ou privés.

Multiple motion encoding in Phase-Contrast MRI: A general theory and application to elastography imaging

Accepted at Medical Image Analysis: https://doi.org/10.1016/j.media.2022.102416

Helge Herthum[1], Hugo Carrillo[2,7], Axel Osses[2,3,4,5]
Sergio Uribe[4,6], Ingolf Sack[1], Cristóbal Bertoglio[7*]

[1]Institute of Medical Informatics, Charité - Universitätsmedizin Berlin,
Corporate Member of Freie Universität Berlin, Humboldt-Universität zu Berlin,
and Berlin Institute of Health, 10117, Berlin, Germany
[2]Center for Mathematical Modeling, Universidad de Chile, Santiago, 8370456 , Chile
[3]Department of Mathematical Engineering , Universidad de Chile, Santiago, 8370456 , Chile
[4]ANID – Millennium Nucleus in Cardiovascular Magnetic Resonance, Santiago, 7820436, Chile
[5]ANID – Millenium Nucleus in Applied Control and Inverse Problems ACIP, Santiago, 7820436, Chile
[6]Biomedical Imaging Center, Pontificia Universidad Católica de Chile, Santiago, 7820436, Chile
[7]Bernoulli Institute, University of Groningen, Groningen, 9747AG, The Netherlands

March 17, 2022

Abstract

While MRI allows to encode the motion of tissue in the magnetization's phase, it remains yet a challenge to obtain high fidelity motion images due to wraps in the phase for high encoding efficiencies. Therefore, we propose an optimal multiple motion encoding method (OMME) and exemplify it in Magnetic Resonance Elastography (MRE) data.

OMME is formulated as a non-convex least-squares problem for the motion using an arbitrary number of phase-contrast measurements with different motion encoding gradients (MEGs). The mathematical properties of OMME are proved in terms of standard deviation and dynamic range of the motion's estimate for arbitrary MEGs combination which are confirmed using synthetically generated data. OMME's performance is assessed on MRE data from in vivo human brain experiments and compared to dual encoding strategies. The unwrapped images are further used to reconstruct stiffness maps and compared to the ones obtained using conventional unwrapping methods.

OMME allowed to successfully combine several MRE phase images with different MEGs, outperforming dual encoding strategies in either motion-to-noise ratio (MNR) or number of successfully reconstructed voxels with good noise stability. This lead to stiffness maps with greater resolution of details than obtained with conventional unwrapping methods. The proposed OMME method allows for a flexible and noise robust increase in the dynamic range and thus provides wrap-free

*Corresponding author: c.a.bertoglio@rug.nl

phase images with high MNR. In MRE, the method may be especially suitable when high resolution images with high MNR are needed.

Contents

1 Introduction **2**

2 Theory **4**
2.1 Single motion encoding . . . 4
2.2 Dual motion encoding . . . 5
2.2.1 Phase-contrast from two MEGs . . . 5
2.2.2 Classical dual motion encoding unwrapping . . . 6
2.2.3 Optimal dual encoding unwrapping . . . 7
2.2.4 Limitations of dual encoding . . . 7
2.3 Optimal multiple motion encoding (OMME) . . . 10
2.4 On the choice of β and N . . . 11

3 Methods **11**
3.1 Subjects . . . 11
3.2 OMME-MRE experimental setup . . . 11
3.3 OMME-MRE sequence . . . 13
3.4 Motion correction and segmentation . . . 14
3.5 Reconstruction of phase contributions . . . 14
3.6 Displacement reconstruction . . . 14
3.7 Shear wave speed reconstruction . . . 15
3.8 Noise reduction by adding back imaging gradient's phase . . . 16
3.9 Noise analysis and statistical tests . . . 16

4 Results **16**
4.1 Phase images . . . 16
4.2 Dual and multiple encoding unwrapping . . . 17
4.3 Comparison to other unwrapping methods . . . 19

5 Discussion **24**

6 Conclusion **25**

A Theoretical and practical aspects of OMME **26**
A.1 Effective dynamic range . . . 26
A.2 Noise analysis . . . 27

1 Introduction

Phase-contrast Magnetic Resonance Imaging (PC-MRI) is a well-established method for measuring flow velocities [1, 2, 3] or tissue displacements due to harmonic excitation as used in Magnetic Resonance Elastography (MRE) [4, 5, 6, 7, 8, 9, 10]. MRE is used for the non-invasive characterization

of the mechanical properties of a specific tissue or organ of interest and has been used for many different applications in pre-clinical animal [11, 12, 13] and in vivo human studies (e.g. cardiac [14, 15], muscle [16, 17], abdomen [18, 19, 20, 21] and brain [22, 23, 24, 25, 26, 27]).

Motion is encoded in the phase of the complex transverse magnetization proportional to the encoding efficiency of the motion encoding gradient (MEG). Yet, the phase can only be measured in the half-open interval $[-\pi, \pi)$ and phase wraps (abrupt jumps of $2\pi k$, with $k \in \mathbb{Z}$) occur if the encoded phase exceeds those limits. Consequently, for a given encoding efficiency, there is a fixed amplitude range or *dynamic range*, where motion can be acquired without phase wraps. In other words, if the encoding efficiency is too large and therefore the true motion amplitude exceeds the dynamic range, phase wraps occur. Unfortunately, selecting a large dynamic range leads to poor quality images since – for a given signal-to-noise-ratio (SNR) in the magnitude image – the "motion-to-noise-ratio" (MNR) is inversely proportional to the dynamic range. Moreover, acquiring and averaging several images with fixed but high dynamic range (i.e. with no wraps) decreases the standard deviation of the averaged image with order $\mathcal{O}(d_G N_G^{-1/2})$, with N_G the number of measurements for a fixed dynamic range d_G.

Therefore, it is a common practice to use low dynamic ranges and then to remove the wraps afterwards. This allows a faster decrease of the standard deviation of the estimated motion encoded image than averaging. There are usually two type of approaches.

First, unwrapping algorithms have been developed by assuming that the motion field is smooth in space, see e.g. [28, 29] and references therein. Nevertheless, they cannot recover the true underlying motion and eventually fail when the aliased regions are highly heterogeneous, subject to noise or include nested wraps (i.e. when $|k| > 1$). In such cases, the unwrapped phase appears to be distorted and obstructs further data processing steps which leads to artifacts in the estimates of tissue properties [10]. For instance, the simple 2π-unwrapping Flynn [30] algorithm is inherently two-dimensional and fails to unwrap noisy complex wraps when no well-defined enclosed region exists. The true motion cannot be recovered because arbitrary 2π-offsets are added. Gradient based algorithms [31] only yield the derivative of the phase and amplify noise. Laplacian based unwrapping algorithms [32] remove the constant and linear terms from the data and induce spatial smoothing, altering the resulting phase where important details may be lost.

Second, voxelwise motion reconstructions using the so called dual motion encoding strategies have been proposed in PC-MRI which are based on unwrapping low dynamic-range data by exploiting high-dynamic range data [33, 34, 35, 36]. In other words, measurements with a reduced dynamic range (hence, improved MNR) are unwrapped using a measurement with a larger dynamic range. Those methods are performed at each voxel independently and therefore they do not assume or enforce smoothness of the motion-encoded phase field. This allows the reconstruction of the correct motion images, but, at the cost of additional measurements. However, dual motion encoding also fails in the presence of noise when the MEG amplitudes do not differ largely.

Hence, the aim of this work is threefold.

Firstly, we analyze dual motion-encoding strategies showing that dual motion encoding methods are limited to low noise phase images.

Therefore, we then develop a mathematical framework for multiple motion encoding, henceforth termed Optimal Multiple Motion Encoding (OMME) as an extension of *optimal dual motion encoding* reported in [35]. We show that OMME outperforms dual motion encoding in terms of unwrapping's robustness to noise. This improvement comes at the cost of additional scans, however being considerably more cost effective in terms of scan time than standard image averaging.

Finally, we propose a MRE scan protocol for OMME and test it on in vivo brain data. We first confirm that OMME provides *either* a more noise robust unwrapping with similar MNR *or* improved MNR with similar noise robustness compared to dual motion encoding strategies. Moreover overcoming the limitations of unwrapping algorithms not only increases MNR but also allows to recover more detailed stiffness maps than using standard unwrapping methods.

2 Theory

In this section, we first introduce the notation and the mathematical model of phase and motion, including theoretical statistical analysis of dual encoding methods. Then, we introduce OMME and derive its statistical properties. Please notice that the theory in this section is formulated for one voxel, one motion encoding direction and one time instance. This means, at the same time, that OMME does not rely on spatio(-temporal) regularity assumptions as conventional unwrapping methods. Therefore, in practice OMME is applied to each direction and spatio-temporal location independently.

2.1 Single motion encoding

For a given MEG "G", the model of measured phase can be written in the form

$$\varphi_G(u) = \delta_G^u + u\frac{\pi}{d_G} + \varepsilon\pi \tag{1}$$

with the following notation:

- u denotes the motion of the media (quantity of interest) in the direction of the MEG (dimensions are velocity or displacement, depending on the quantity encoded);
- d_G is the "dynamic range" of motion encoding, which depends on the MEG's amplitude, duration, shape and assumption on the motion (same dimensions as u);
- δ_G^u is the spatially varying background phase, which in general depends on gradient imperfections of spin-echo sequences, the MEG (e.g by eddy currents and Maxwell effects) and the motion since imaging gradients also encode motion (time dependent);
- ε is a zero mean Gaussian random variable representing the measurement noise in the phase. Its variance depends on the SNR of the magnitude measurements.

The background phase can further be modelled as follows:

$$\delta_G^u = \varphi_0 + \delta_G + m(u) \tag{2}$$

with the following notation:

- φ_0 is the time constant (static) background phase of the imaging gradients due to gradient imperfections and concomitant fields
- δ_G is a time constant MEG-dependent phase induced e.g by eddy currents and Maxwell effects
- $m(u)$ is the motion-dependent phase encoded by the imaging gradients.

In order to separate the unwanted background phase from the desired dynamic (time dependent) contributions of the MEG, it is necessary to perform a series of acquisitions with and without applied vibrations and MEGs. In flow velocity–encoded MRI, the measurement of δ_G^u is the common practice (i.e. four points 4D Flow) [2]. In MRE, we will show in the methods section that δ_G^u can be measured considerably faster compared to $\varphi_G(u)$.

We define as *single encoding* the situation where u estimated from a measurement of the background phase δ_G^u and the full phase $\varphi_G(u)$, for a single MEG G.

Given measurements of $\varphi_G(u)$ and δ_G^u with noise realizations ε_u and ε_δ, respectively, the single-encoding estimation u_G is given by:

$$u_G = (\varphi_G(u) - \delta_G^u)\frac{d_G}{\pi} - (\varepsilon_u - \varepsilon_\delta)d_G. \tag{3}$$

For the sake of generality, we will assume different distributions for ε_u and ε_δ, i.e. $\varepsilon_u \sim \mathcal{N}(0, \sigma_\varphi^2)$, $\varepsilon_\delta \sim \mathcal{N}(0, C_\delta^2\sigma_\varphi^2)$, $C_\delta \geq 0$ and $\mathrm{Cov}(\varepsilon_u, \varepsilon_\delta) = 0$, i.e. they are independent random variables. The constant C_δ represents the proportion in standard deviations between the motion-encoded phase and the background phase measurements, which may differ in practice. Consequently, $u_G \sim \mathcal{N}(u_{true}, (1 + C_\delta^2)d_G^2\sigma_\varphi^2)$, with u_{true} the true motion.

Therefore, for a fixed value of σ_φ, d_G should be chosen as small as possible in order to minimize $\mathrm{Var}(u_G)$. However, phase can be measured only within the interval $[-\pi, \pi)$. Hence, if $d_G < |u_{true}|$ (if $\sigma_\varphi = 0$) then u_G wraps by a multiple of $2d_G$. Wraps can also occur even if $d_G > |u_{true}|$ in the presence of noise $\varepsilon \neq 0$.

For a given dynamic range d_G, a possible approach to reduce $\mathrm{Var}(u_G)$ is to average more measurements, say n_G times. Then:

$$u_G \sim \mathcal{N}(u_{true}, (1 + C_\delta^2)d_G^2\sigma_\varphi^2 n_G^{-1}). \tag{4}$$

From this relation it is clear that decreasing d_G is more effective than increasing the number of measurements n, since $\mathrm{Var}(u_G)$ decreases with d_G^2/n_G.

2.2 Dual motion encoding

2.2.1 Phase-contrast from two MEGs

We assume now that we measure phases with two different MEGs amplitudes $G_1 \neq G_2 = G_1/\beta$, with $\beta \neq 0$. Without loss of generality, we assume $0 < \beta < 1$, obtaining dynamic ranges d_1 and $d_2 = \beta d_1$, respectively. This results in four measured phases $\varphi_1, \delta_1^u, \varphi_2, \delta_2^u$. We assume that these values already include the additive noise as indicated above. We also assume for the subsequent computation of the variances that these phases have no wraps.

From the four phase measurements, four motion images can then be estimated:

$$u_1 = \frac{\varphi_1 - \delta_1^u}{\pi}d_1 \ , \ u_2 = \frac{\varphi_2 - \delta_2^u}{\pi}d_2 \tag{5}$$

$$u_{ps} = \frac{\varphi_1 + \varphi_2 - \delta_1^u - \delta_2^u}{\pi}d_{ps} \ , \ u_{pc} = \frac{\varphi_2 - \varphi_1 + \delta_1^u - \delta_2^u}{\pi}d_{pc} \tag{6}$$

with $d_{ps} = (d_1^{-1} + d_2^{-1})^{-1}$, $d_{pc} = (d_2^{-1} - d_1^{-1})^{-1}$. The indexes pc and ps denote *phase contrast* and *phase sum*, respectively. Notice that

$$\begin{cases} d_{pc} = d_1 \dfrac{\beta}{1-\beta} \geq d_1 > d_2 = \beta d_1 > d_{ps} = d_1 \dfrac{\beta}{1+\beta}, & \text{for } 1/2 \leq \beta < 1, \\ d_1 > d_{pc} = d_1 \dfrac{\beta}{1-\beta} > d_2 = \beta d_1 > d_{ps} = d_1 \dfrac{\beta}{1+\beta}, & \text{for } 0 < \beta < 1/2 \end{cases} \tag{7}$$

Defining $\alpha = C\sigma_\varphi d_1$, with $C = \sqrt{(1 + C_\delta^2)}$, the variances of the different motion estimators satisfy:

$$\mathrm{Var}(u_1) = C^2\sigma_\varphi^2 d_1^2 = \alpha^2 \ , \ \mathrm{Var}(u_2) = C^2\sigma_\varphi^2 d_2^2 = \alpha^2\beta^2 \tag{8}$$

$$\mathrm{Var}(u_{pc}) = 2C^2\sigma_\varphi^2 d_{pc}^2 = \alpha^2 \frac{2\beta^2}{(1-\beta)^2} = \alpha^2 \frac{\beta^2}{\left(\dfrac{1-\beta}{\sqrt{2}}\right)^2} \tag{9}$$

$$\mathrm{Var}(u_{ps}) = 2C^2\sigma_\varphi^2 d_{ps}^2 = \alpha^2 \frac{2\beta^2}{(1+\beta)^2} = \alpha^2 \frac{\beta^2}{\left(\dfrac{1+\beta}{\sqrt{2}}\right)^2}. \tag{10}$$

2.2.2 Classical dual motion encoding unwrapping

As explained above, when the dynamic ranges are decreased, wraps appear. Dual encoding reconstructions aim to unwrap a motion u_{low} obtained with low dynamic range d_{low} using a motion u_{high} obtained with a high dynamic range d_{high} as follows [33]:

$$u_{uw} = u_{low} + 2d_{low} N.I. \left(\frac{u_{high} - u_{low}}{2d_{low}} \right) \tag{11}$$

with $N.I.$ the nearest integer operator. This leads to $\mathrm{Var}(u_{uw}) = \mathrm{Var}(u_{low})$ when the unwrapping is successful. This method will be denoted in as *standard dual encoding*. We denote as *effective dynamic range* of the dual motion encoding unwrapping method $d_{eff} = d_{high}$.

To choose u_{low} and u_{high} we apply the following reasoning. Firstly, we select $u_{low} = u_2$ since it possess a higher dynamic range than u_{ps} (e.g. $d_{pc} = 3/2 d_{ps}$ for $\beta = 1/2$) only with a slightly higher variance (e.g. $\mathrm{Var}(u_2)/\mathrm{Var}(u_{ps}) = 1.125$ for $\beta = 1/2$). Secondly, we select

$$u_{high} = \begin{cases} u_1 & \beta = 1 \\ u_{pc} & \dfrac{1}{2} < \beta < 1 \\ u_1 & 0 < \beta \leq \dfrac{1}{2} \end{cases} \tag{12}$$

since u_{pc} has the desired effective range $d_{pc} = d_{eff} \geq d_1$ for $\beta > 1/2$, but for $\beta \leq 1/2$ it holds $d_1 = d_{eff}$, and for $\beta = 1$ u_{pc} is not defined and $d_1 = d_{eff}$.

Remark 1 *Note that a dual encoding approach presented in [36] – with both MEGs chosen with different polarity, i.e. differing by a factor $-k$, with $0 < k < 1$ – is equivalent to the one defined above. Indeed, it can be shown that for a fixed d_{eff} its lowest dynamic range corresponds to $d_{pc} =$*

$(1-k)/(1+k)d_{eff}$. *Then, the lowest dynamic range is* $d_2 = d_{eff}(1-\beta)$. *This leads to both approaches be equivalent if* $\beta = 1 + (k-1)/(k+1)$. *In [36], it was for instance taken* $k = 0.777$ *hence equivalent to a* $\beta = 0.875$. *Note that we excludes the case* $k = 1$ *from the analysis since it does not correspond formally to dual encoding but to single encoding because* $d_{ps} \to \infty$.

2.2.3 Optimal dual encoding unwrapping

In [35], a new method for unwrapping two motion-encoded images was introduced, *Optimal Dual Venc* (ODV). The method is based on the formulation of the phase contrast problem as the minimization of cost functional. For the single motion encoding case, the cost functional has the form:

$$J_i(u) = 1 - \cos\left(\varphi_i - \delta_i^u - \frac{\pi u}{d_i}\right) = 1 - \cos\left(\frac{\pi}{d_i}(u_i - u)\right) \tag{13}$$

which comes from a least squares approximation for the angle by measuring the components of a vector.

It is easy to see that the period of $J_i(u)$ is $2d_i$, and therefore local minimum among with smallest value (in absolute terms) $u_i + 2k_i d_i, k_i \in \mathbb{Z}$, corresponds to the the single encoding phase-contrast motion.

For the dual encoding case, the problem shifts from finding the local minima of $J_i(u)$ to find the global minima of

$$J_{dual}(u) = J_1(u) + J_2(u) = 2 - \cos\left(\frac{\pi}{d_1}(u_1 - u)\right) - \cos\left(\frac{\pi}{d_2}(u_2 - u)\right). \tag{14}$$

It was proven in [35] that u_{true} is a global minimum of J_{dual} in the noise-free case. Now in Appendix A.1, we prove that in the general case – and possibly with noisy data – unwrapping is produced by the fact $d_{dual} = lcm(d_1, d_2)$, with lcm the least common multiplier function, is the minimal value such that $J_{dual}(u) = J_{dual}(u + d_{dual})$ when $d_1/d_2 \in \mathbb{Q}$. . Moreover, it can be also noted that $d_{dual} = d_{eff}$. Indeed, writing $\beta = a/b, a < b \in \mathbb{N}$ we obtain

$$d_{eff} = d_1 \frac{a/b}{1 - a/b} = d_1 \frac{a}{b-a}\ ,\ d_{dual} = d_1 a \tag{15}$$

where the last equality follows from the proof in Appendix A.1. If $b = a + 1$, then $d_{eff} = d_{dual}$. Also by definition, if $\beta < 1/2$, then $d_{eff} = d_{dual} = d_1$. Therefore, in these scenarios both standard dual encoding and ODV methods have the same effective dynamic range and they can be fairly compared to each other.

Another contribution of this work is the computation of the variance of the ODV estimate u_* leads to

$$\mathrm{Var}(u_*) = \frac{\mathrm{Var}(u_2)}{1 + \beta^2} < \mathrm{Var}(u_2) \tag{16}$$

The computation is detailed in Appendix A.2 for the more general case of multiple encoding.

2.2.4 Limitations of dual encoding

From Equation (7), notice that when $\beta \to 1^-$ (left limit), then $d_{eff} \to \infty$. Therefore, one may think that d_1, d_2 could be chosen arbitrarily small to minimize $\mathrm{Var}(u_1), \mathrm{Var}(u_2)$ while keeping d_{eff}

large. However, we will show here that noise affects the unwrapping performance of the methods. Therefore, dual motion encoding strategies have limitations which become more important the closer d_1 and d_2 are.

Figure 1 presents the previous findings in a graphical way. There, we show the standard deviations of the estimators (i.e. the square root of the variances) versus the effective dynamic ranges for various values of β. Each sub-figure was generated for a given value of $\beta \in \{1/4, 1/2, 2/3, 3/4, 1\}$ and $\sigma_\phi = \{0.01, 0.05\}$, by the following procedure:

- Ground truth values are set as: $u_{true} = 1$ and $\delta_1^u = \delta_2^u = 0.9\pi$.
- For a fixed value of d_{eff} and β, d_1 are computed as:

$$d_1 = \begin{cases} d_{eff} & \text{if } \beta = 1, \beta \leq 1/2 \\ d_{eff}\dfrac{1-\beta}{\beta} & \text{if } 1/2 < \beta < 1 \end{cases} \tag{17}$$

- Measurements of motion encoded phases φ_1, φ_2 were generated using Equation (1), the ground truth values of the parameters defined above and adding Gaussian noise with standard deviation σ_φ. Measurements were wrapped to the interval $[-\pi, \pi]$.
- δ_1^u, δ_2^u are perturbed adding Gaussian noise with standard deviation σ_φ.
- Then u_1, u_2 were computed with Equation (5). Phase differences were wrapped to the interval $[-\pi, \pi]$.
- u_{uw} with Equation (11) and u_* with the algorithm detailed in Equation (21).
- Similarly u_{eff} was generated being the single motion phase contrast estimate with $d_G = d_{eff}$ is computed for comparison.
- The standard deviation of such estimates considering the 5000 realizations is computed.
- The curves are drawn by repeating this procedure in the interval $d_{eff} \in [1, 4]$.
- The theoretical standard deviations curves are the ones following the derivations in the previous sections: $\sqrt{2}d_{eff}\sigma_\varphi$ (single encoding), $\sqrt{2}d_2\sigma_\varphi$ (standard dual encoding) and $\sqrt{2}d_2/\sqrt{1+\beta^2}\sigma_\varphi$ (ODV).

The quality of the results depends on both values of β and σ_φ. For small values of σ_φ, the empirical and theoretical standard deviations match, but the empirical increases – deviating from the theoretical one – when $d_{eff} \to |u_{true}|$, as expected, due to the wraps. This issue becomes more relevant when σ_φ grows. In this low noise scenario, the maximum gain with respect to the case of repeating the same measurements (i.e. $\beta = 1$) is when $\beta = 3/4$ since for a fixed d_{eff}, $d_1 = d_{eff}/3$ and $d_2 = d_{eff}/4$.

However, the reconstruction with $\beta = 3/4$ becomes unstable when increasing σ_φ. A similar effect can be observed with $\beta = 1/2$. The most robust variant with respect to noise for both standard and optimal methods appears to be $\beta = 1/2$, where $d_1 = d_{eff}$ and $d_2 = d_{eff}/2$. In case of the optimal method, this can be explained by the fact that the local minima of both J_1 and J_2 cost functionals have maximal distance. For the other values of β, this distance is much smaller, we refer to [35] for details.

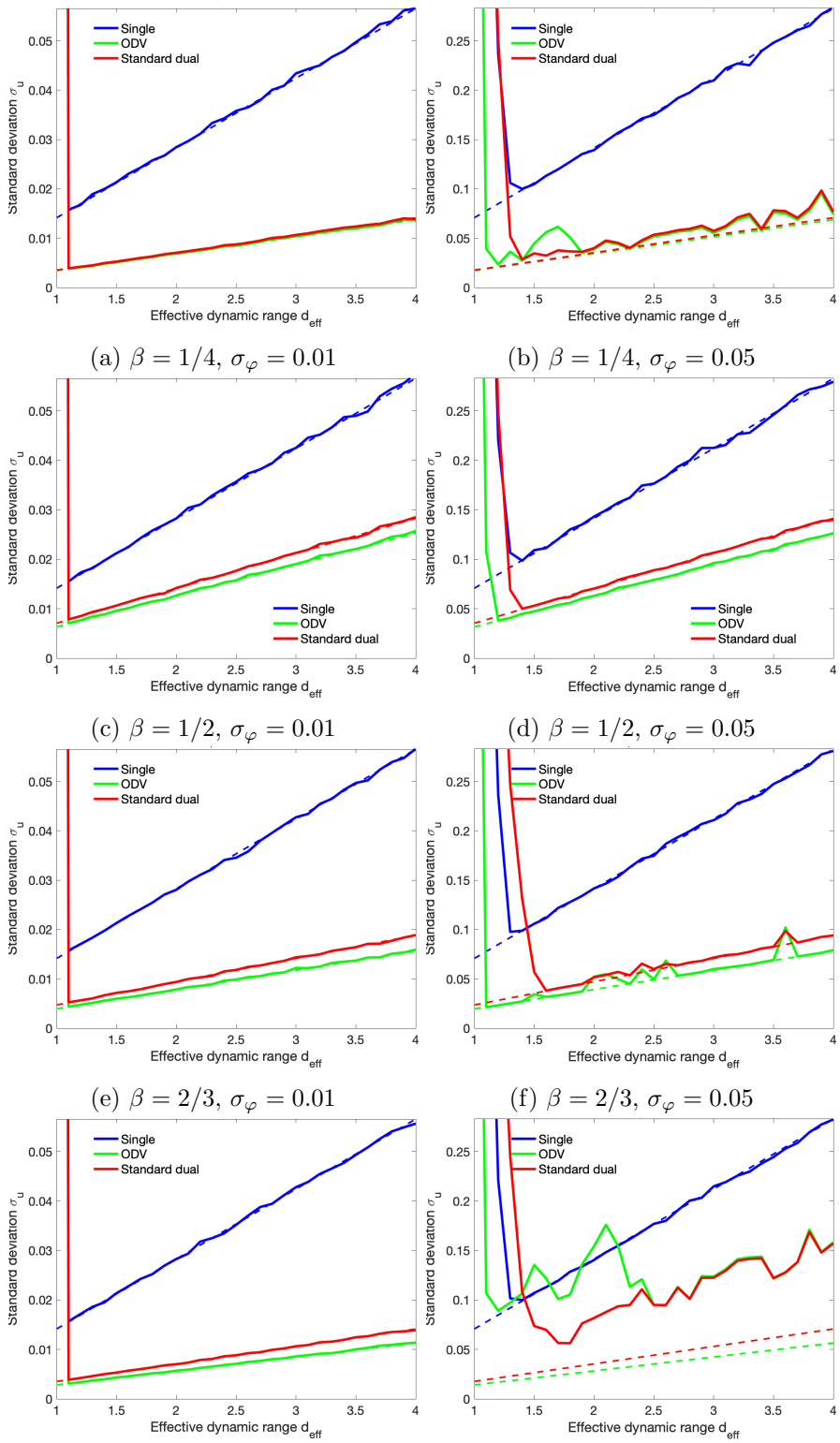

(a) $\beta = 1/4$, $\sigma_\varphi = 0.01$ (b) $\beta = 1/4$, $\sigma_\varphi = 0.05$

(c) $\beta = 1/2$, $\sigma_\varphi = 0.01$ (d) $\beta = 1/2$, $\sigma_\varphi = 0.05$

(e) $\beta = 2/3$, $\sigma_\varphi = 0.01$ (f) $\beta = 2/3$, $\sigma_\varphi = 0.05$

(g) $\beta = 3/4$, $\sigma_\varphi = 0.01$ (h) $\beta = 3/4$, $\sigma_\varphi = 0.05$

Figure 1: Standard deviations v/s effective dynamic range for single and dual encodings for $\beta = \{1/4, 1/2, 2/3, 3/4\}$ (from top to bottom) and $\sigma_\varphi = \{0.01, 0.05\}$ (from left to right). Continuous lines represent the empirical ones (i.e. computed from the numerical experiments) and dashed lines the theoretical ones given in the last bullet point in Page 8.

In particular for $\beta = 1/2$, between both methods, the optimal dual encoding appears to be more robust with respect to noise, especially when $d_{eff} \to |u_{true}|$, and slightly better than the standard dual encoding approach when $d_{eff} > |u_{true}|$ due to (33). The possible explanation is that unwrapping and noise compensation are done simultaneously, and therefore, a more robust unwrapping method results. For other values of β, it appears that the standard dual approach performs better in terms of robustness when $d_{eff} \to |u_{true}|$.

2.3 Optimal multiple motion encoding (OMME)

We now propose a systematic method to include N measurements with dynamic ranges $d_1, \ldots, d_N$ in order to extend the effective dynamic range d_{eff} while keeping $\mathrm{Var}(u_*)$ as the one for the smallest $d_1, \ldots, d_N$. The idea is that by doing so, we can increase the robustness of the unwrapping when σ_φ increases. Therefore, such strategy can be of great utility when high quality images are needed e.g. at high spatial resolutions, for instance.

The optimal dual encoding formulation allows a straightforward extension to multiple MEGs, i.e.

$$J_N(u) = \sum_{j=1}^{N} \left(1 - \cos\left(\frac{\pi}{d_j}(u_j - u)\right)\right) \tag{18}$$

The multiple motion encoding reconstruction u_* is then the global minimum of smallest magnitude within $[-d_{eff}, d_{eff}]$, with d_{eff} the dynamic range of OMME. From the proof in Appendix A, J_N has periodicity equal to the least common multiplier of $2d_1 = \cdots = 2d_N$ when $d_j = d_1(a/b)^{j-1}, a < b \in \mathbb{N}$, being then $d_{eff} = a^{N-1}d_1$ half of that periodicity.

The variance of u_*, is given by

$$\mathrm{Var}(u_*) = \mathrm{Var}(u_N)\frac{1-\beta^2}{1-\beta^{2N}} < \mathrm{Var}(u_N), \tag{19}$$

see detailed computation in Appendix A.2. For instance for the case of $\beta = 1/2$ – which is the most robust as it was shown above – the reductions are for $N = 2, 3, 4$

$$\sqrt{\mathrm{Var}(u_*)} = 0.89\sqrt{\mathrm{Var}(u_2)}, \sqrt{\mathrm{Var}(u_*)} = 0.87\sqrt{\mathrm{Var}(u_3)}, \sqrt{\mathrm{Var}(u_*)} = 0.86\sqrt{\mathrm{Var}(u_4)}, \tag{20}$$

respectively. Therefore, the gain in noise reduction with respect to the lowest dynamic range is only slightly reduced. At the same time, the computational complexity of the an exhaustive search of the global minimum of $J_N(u)$ increases considerably with N, since the the interval $[-d_{eff}, d_{eff}]$ needs to be sampled according to d_N. Therefore, we propose here to just use $J_N(u)$ to guide the unwrapping of u_N, i.e. to find u_* by solving:

$$k_* = \arg\min_{k\in\mathbb{Z}} J_N(u_N + 2d_N k), \text{ subject to } -d_{eff} \le u_N + 2d_N k \le d_{eff} \tag{21}$$

and then to set $u_* = u_N + 2d_N k_*$. This leads to $\mathrm{Var}(u_*) = \mathrm{Var}(u_N)$. For image datasets as used in this work, e.g. for $N = 3$ solving Problem (21) is about 9 times faster than an exhaustive global minimum search of $J_N(u)$.

Figure 2 shows the results OMME using a number of measurement combinations, values of β and σ_ϕ. For $\beta \neq 1$, the fast version of OMME was used, while for $\beta = 1$ the standard version of OMME which averages the phases in the complex plane.

It can be appreciated that, when $\beta \neq 1$, OMME with $\beta = 1/2$ provides the most robust unwrapping with respect to noise. It can be also seen that when further increasing the noise σ_φ, OMME decreases its robustness. It can also appreciated that, for $\beta = 1/2, 1$, increasing N also increases the robustness when $d_{eff} \to u_{true}$ for each level of noise.

Of course, the unwrapping capabilities of OMME fail when the noise grows. In that case, it is recommendable to just repeat the experiment with the same dynamic range and average the results, as done for instance in Figure 2f. This of course provides only a linear decrease in the variance with respect to the number of measurements N, as shown in Figure 2, instead of exponential as in OMME. Naturally, both strategies could be eventually combined (if enough scan time available) by averaging first for each MEG and then use OMME with $\beta = 1/2$ with a better SNR.

2.4 On the choice of β and N

If the user sets the desired dynamic range d_{eff} (e.g. 20 μm in MRE), as presented above the best combination of β and N depends on σ_φ.

If the dynamic range at the desired MNR is d_N, and we fix the proportion $\beta = a/b$, the number of gradients can be found by using the relation

$$d_{eff} = d_1 a^{N-1} = \frac{d_N}{\beta^{N-1}} a^{N-1} = d_N b^{N-1} \tag{22}$$

leading to $N = \log(d_{eff}/d_N)/\log(b) + 1$.

For example, if $d_{eff}/d_N = 8$, then with $\beta = 1/2$ $N = \log(8)/\log(2) + 1 = 4$, and with $\beta = 2/3$ $N = \log(8)/\log(3) + 1 = 2.89 \approx 3$. Notice also that for $\beta > 1/2$, this implies that $d_1 < d_{eff}$ and hence the d_1 image can still contain wraps while d_{eff} may not. However, what we recommend is first to take $\beta = 1/2$, which provides the best unwrapping robustness when increasing SNR: in the next sections we show that in real MRE images $\beta > 1/2$ often fails already when $N = 2$.

3 Methods

3.1 Subjects

In vivo MRE was performed in eight healthy men without a history of neurological diseases (mean age $\pm$ SD: 36 ± 9 years). The study was approved by the ethics committee of Charite-Universitaetsmedizin Berlin in accordance with the Ethical Principles for Medical Research Involving Human Subjects of the World Medical Association Declaration of Helsinki. Every participant gave written informed consent.

3.2 OMME-MRE experimental setup

All experiments were performed in a 3T MRI scanner (Siemens Magnetom Lumina, Erlangen, Germany). In order to separate the different contributions to the background phase as indicated in Equations (1) and (2), four scans were consecutively acquired in each subject as summarized in Table 1.

Measurements with harmonic vibrations sampled eight phase offsets equally spaced over a vibration period using pressurized air drivers as described elsewhere [37]. The vibrations were induced with a forerun of 2 s before MRE data acquisition was started in order to establish a steady state of

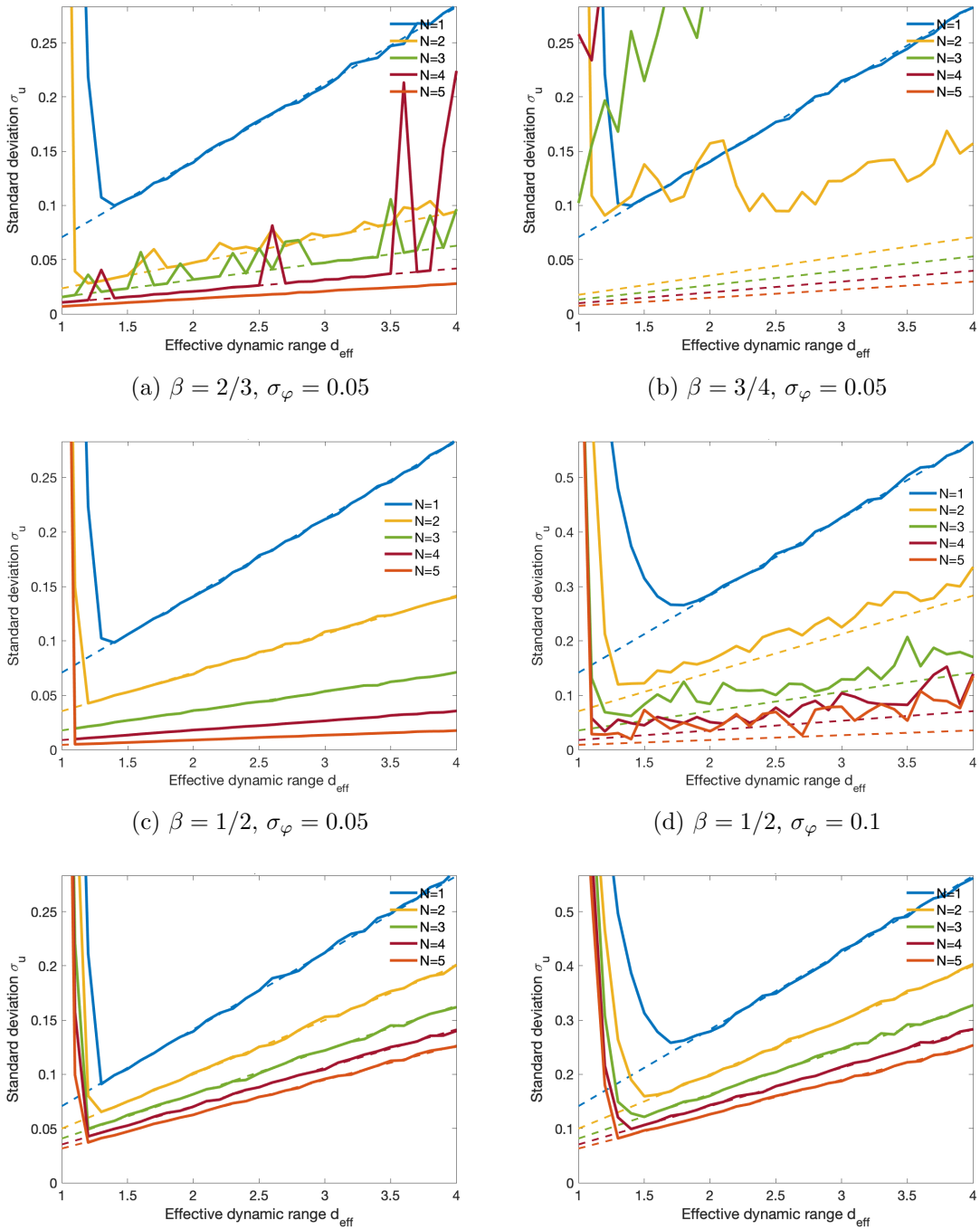

(a) $\beta = 2/3$, $\sigma_\varphi = 0.05$

(b) $\beta = 3/4$, $\sigma_\varphi = 0.05$

(c) $\beta = 1/2$, $\sigma_\varphi = 0.05$

(d) $\beta = 1/2$, $\sigma_\varphi = 0.1$

(e) $\beta = 1$, $\sigma_\varphi = 0.05$

(f) $\beta = 1$, $\sigma_\varphi = 0.1$

Figure 2: Standard deviation v/s effective dynamic range for the OMME reconstruction for $\beta = \{1/2, 2/3, 3/4, 1\}$ with $N = 1, \ldots, 5$ for $\sigma_\phi = 0.05$ (as the worst case in the previous Figure 1) and for $\beta = \{1/2, 1\}$ with $\sigma_\phi = 0.1$. The continuous lines represent the empirical results (i.e. the one computed from the numerical experiments) and the dashed lines the theoretical results.

Phase contribution	Vibration	MEG	Timesteps	Directions	Scan time [norm]
1. $\varphi_G(u)$	on	on	8	3	1
2. φ_0	off	off	1	1	1/24
3. $\varphi_0 + \delta_G$	off	on	1	3	1/8
4. $\varphi_0 + m(u)$	on	off	8	1	1/3

Table 1: Measurement strategy for determining different phase contributions and for the dual motion encoding and OMME reconstructions.

time-harmonic oscillations throughout the brain. Measurements with active MEGs were conducted for three spatial directions along head-feet, left-right and anterior-posterior consecutively and were repeated for each single MEG amplitude. The amplitude of the harmonic vibrations was the same in all individual acquisitions. It was tuned to avoid signal voids due to intra-voxel phase dispersion for the highest MEG amplitude and to not show any phase wraps for the MEG amplitude of 8 mT/m. In three subjects the measurement without vibration was repeated once with same MEG polarity (δ_{G+}) and once with opposite MEG polarity (δ_{G-}) to investigate the influence of MEG polarity on the induced static background phase and further detailed in section 3.5.

Using the same polarity has an advantage when doing dual multiple encoding. For a given dynamic range d_G, either $\{-G/2, G/2\}$ (symmetric) or $\{G$,background$\}$ (non-symmetric) need to be measured to perform the phase contrast and remove the background phase. In dual or multiple-encoding, this needs to be done before the reconstruction and not afterwards e.g. by the Fourier analysis.

With regard to table 1 it can be appreciated that if, one full MEG measurement requires 1 scan time unit, the symmetric phase-contrast approach requires 2 while the latter would require $1+1/3+1/8+1/24 = 1.5$, hence being more time-effective already for one single motion encoding. Of course, the symmetric approach has the advantage of being able to decrease the dynamic range with the same MEG amplitude, hence potentially being able to obtain better MNR (but more wraps). Also, it only performs two subtractions, instead of 4, leading to a better MNR. However, the MNR of the non-symmetric approach can be brought to the value of the symmetric case when ϕ_0 is smoothed and the imaging gradients are neglected for large MEGs as it is presented later in Section 3.8.

In multiple encoding, for N dynamic ranges, the symmetric approach would lead to $2N$ scan time units. The non-symmetric approach, would lead to $N + 1/3 + N/8 + 1/24 = N(9/8) + 9/24$ scan time units. This is a considerable advantage in terms of scalability of the non-symmetric approach with respect to the symmetric one.

3.3 OMME-MRE sequence

Single frequency MRE using a single-shot, spin-echo echo-planar imaging (EPI) sequence was performed for harmonic vibrations at 31.25 Hz. 17 axial slices with an interslice gap of twice the slice thickness were recorded using GRAPPA parallel acquisition [38] with acceleration factor of 2. Slice positioning was automatically done using the scanner build-in auto align function based on the localizer scan (head-brain). Further imaging parameters were: field of view 202 x 202 mm^2, voxel size 1.6 x 1.6 x 1.6 mm^3, echo time (TE) of 74 msec and repetition time (TR) of 2500 msec. Three components of the wavefield in orthogonal directions were acquired with first order flow-

compensated MEGs of varying amplitude (32, 24, 16, 8, 4, 2 mT/m) and a fixed frequency of 34 Hz with slew rate of 125 mT/m/ms. The corresponding dynamic ranges were 7, 9, 13, 26, 52, 104 μm. The dynamic range of the imaging gradients was 149 μm. Each time the MEG amplitude was changed, one preparation scan was performed to reduce transient effects of eddy-currents.

Acquisition time for a set of 3D MRE data was approximately 6:55 min (70s per MEG amplitude, vibration on and MEG on). Additional acquisition time for the individual background phase contributions was 3:07 min.

3.4 Motion correction and segmentation

Complex MR images were corrected for stochastic head motion in the range of ± 2 mm using SPM12 [39]. Moreover measurements without vibration were registered to corresponding measurements with vibration, since deflated actuators results in a vertical displacement of axial slices in the order of 1-2 mm with respect to the inflated actuators during vibration. Automatic segmentation of white matter (WM) and gray matter (GM) based on averaged MRE magnitude images was done using SPM12. The tissue probability maps were thresholded at 0.8 for WM and 0.9 for GM to generate logical tissue-associated voxel masks. The GM threshold was higher to reduce boundary artifacts at cortical GM/fluid boundaries (see Figure 3).

3.5 Reconstruction of phase contributions

The individual phase contributions in Equation (2) were recovered by a number of subtractions. φ_0 (measurement 2, see Table 1) was subtracted from measurement 3 to determine the static MEG-dependent phase δ_G. Subtraction of measurement 3 (φ_0) and measurement 4 gave the motion-dependent phase encoded by the imaging gradients $m(u)$. The static background phase components φ_0 and δ_G were smoothed using a Gaussian filter with 1 mm standard deviation in order to reduce noise enhancement by further subtraction of these components. This was justified since both static phases show low spatial variations within the brain. Finally we subtracted the individual phase contributions from measurement 1 to determine the tissue displacement encoded by the MEG only (1). From the repeated measurements without vibrations and either same or opposite MEG polarity, we determined pixel-wise the relative absolute error (RAE) ($RAE_+ = |\delta_{G+} - \delta_{G+}|/\pi; RAE_- = |\delta_{G+} - \delta_{G-}|/\pi$). The RAE was then averaged over WM and GM and subjects for each MEG amplitude.

3.6 Displacement reconstruction

Single encoding phase contrast images were computed for each MEG using Equation (3) (assuming no noise). The background phase was obtained as detailed in Section 3.5. Dual and tri-encoding phase images were computed using the OMME formula (21). Dual encoding phase images were computed using the combinations of two single encoding images, namely 32 and 24 mT/m, 24 and 16 mT/m, 16 and 8 mT/m, 32 and 8 mT/m. In addition, OMME was used to combine three phase images acquired with MEG amplitudes of 32, 16, 8 mT/m and 32, 24, 16 mT/m.

As shown in the theory section all these combinations exhibit the same dynamic range d_G given by the lowest encoding amplitude of 8 mT/m, which had no more phase wraps. Notice that due to the inclusion of $m(u)$ in the background phase for all MEGs, the phase difference measurements are not i.i.d. as assumed in the noise analysis. However, recall that Equation (21) is used for the

reconstruction and therefore the unwrapped image does not result in the combination of phase differences any more. Therefore, the measurements not being i.i.d. does not affect the variance of the reconstruction.

We determined the number of wrongly reconstructed voxel inside WM and GM tissue for each combination of MEG amplitudes in order to assess the noise sensitivity of the different combination possibilities in vivo as it was simulated before (see Figure 1). We defined the single phase-contrast image with a MEG of 8 mT/m as our ground truth and calculated the voxel wise difference to the multiple MEG phase reconstructions. Based on the noise level in the image and the maximum encoded displacement, a threshold of 0.1 rad phase difference was used to identify wrongly reconstructed voxel in WM and GM. Relative error rates were determined by dividing the number of wrongly reconstructed voxels by the total number of voxels included in the GM and WM masks in all slices, timesteps and encoding directions.

To further investigate the noise sensitivity of the displacement reconstruction, we added complex Gaussian noise with a standard deviation of 15% of the mean absolute encoded phase in WM and GM to the single PC images and repeated the evaluations.

Furthermore wrapped single motion encoding phase contrast images for the highest MEG of 32 mT/m were unwrapped using Laplacian and Flynn based unwrapping algorithms. We chose to compare our proposed method with Flynn and Laplacian based unwrapping to include two common but different approaches which are publicity available at `https://bioqic-apps.charite.de`. We compared the different unwrapping approaches in terms of MNR as described further below and in terms of the visual quality of the reconstructed elastograms as outlined in the next section.

3.7 Shear wave speed reconstruction

Wrap-free phase images from unwrapping algorithms and from dual and multiple encoding methods were used for reconstruction of shear wave speed (SWS) maps based on phase-gradient wavenumber recovery to avoid noise amplification by the Laplacian operator which is inevitable in direct inversion techniques [40, 41]. SWS is related to tissue stiffness and will be termed as such in the following. The principle of wavenumber (k-) based multi-component, elasto-visco (k-MDEV) inversion was originally introduced for liver MRE and is outlined in [42].

It is important to note that each reconstructed voxel of the elastograms resulted directly from 24 individual voxels of the phase images (8 timesteps and three encoding directions) and indirectly from their surrounding voxels as well. If only one voxel in the phase images is wrongly reconstructed, the resulting elastogram voxel is corrupted. Therefore we analysed additionally the wrongly reconstructed voxels with respect to the elastograms for the comparison of different multiple encoding approaches. To calculate relative error rates, we divided again the number of wrongly reconstructed voxels by the number of all directly affecting voxels. In contrast to the phase images, the number was not multiplied by the amount of timesteps and encoding directions.

k-MDEV inversion was adapted to the resolution of brain MRE as outlined in [43]. Compared to k-MDEV proposed for abdominal organs [42], smoothing the phase images prior to the unwrapping was omitted since this would have influenced the MNR estimations. Moreover, the linear radial filter in the spatial frequency domain was replaced by a radial bandpass Butterworth filter of third order with highpass threshold of 15 1/m and lowpass threshold of 250 1/m.

3.8 Noise reduction by adding back imaging gradient's phase

In the OMME context, the subtraction of $m(u)$ is needed for the correct phase contrast when including several gradient strengths. However, it is a common practice to assume that the phase contribution $m(u)$ is small with respect to the contribution of the wave motion for the largest MEG (i.e. smallest dynamic range d_N). In such cases adding back the phase contribution of the imaging gradient's to the OMME reconstruction allows theoretically for a reduction factor $1/\sqrt{2} \approx 0.7$ in the standard deviation of the noise of the displacement field.

Therefore, the displacements obtained with OMME are postprocessed by the following operation

$$u_* \to u_* + \frac{m(u)}{\pi} d_N \tag{23}$$

This effect is compared quantitatively in terms of MNR as outlined in the next section and qualitatively on the resulting elastograms in Figure 5. All other results, elastograms and wave fields are without re-added m(u).

3.9 Noise analysis and statistical tests

Signal power and MNR of the phase images are important parameters for the subsequent post-processing and final SWS reconstruction. According to our theory, OMME promises wrap-free phase images with MNR corresponding to the highest MEG used for OMME phase recovery. To calculate MNR for experimental data (unwrapped and unsmoothed phase images) we used the blind noise estimation method from [44] as outlined and previously applied to MRE data in [45]. Noise estimation in the wavelet domain is expected to be well suited for wave images [46, 47]. We estimated MNR from the dual-tree wavelet transformation of the displacement images with the median absolute deviation of the finest band of wavelet coefficients [44]. The estimated signal power was derived from the L2-norm. Signal and noise levels were estimated from automatically segmented WM and GM regions (see Figure 3) for all slices and components and averaged afterwards.

To test for significant differences in the number of reconstruction failures using OMME and dual encoding strategies, a linear mixed-effects model with varying intercept was employed. Error rates were used as dependent variables and the different methods as independent variables. Participants were assigned as random effect. To test for significant differences in the MNR of unwrapped phase images using OMME, Laplacian and Flynn unwrapping, a linear mixed-effects model with varying intercept was employed. MNR was used as dependent variables and the different methods as independent variables. Participants were assigned as random effect. All P-values were calculated using Tukey's *post hoc* test with Bonferroni correction for multiple comparisons. All statistical analysis was done in R (version 4.0.2). Unless otherwise stated, errors are given as standard deviation (SD). P-values below 0.05 were considered statistically significant.

4 Results

4.1 Phase images

Figure 3 shows the encoded phase of the complex MR signal, with the different contributions modeled by Equations (1) and (2) derived from the measurements listed in Table 1. One central slice of the anterior-posterior encoding direction is displayed for one representative subject. The

third column shows the static background phase induced by toggled MEGs. For reference the MRE mean magnitude and masks for WM and GM are given. Table 2 summarizes the encoding efficiency for the different MEG amplitudes and the imaging gradients. Group mean absolute displacement for all encoding directions averaged over WM tissue in rad is given. Furthermore the averaged RAE of the background phase for the same and opposite MEG polarity is tabled, RAE_+ and RAE_- respectively. The encoded phase $u\frac{\pi}{d_G}$ increased with increasing MEG amplitude and phase wraps occurred from 16 mT/m on. The static background phase induced by the MEG δ_G decreased with amplitude until no difference compared to the background phase induced by the imaging gradients φ_0 was visible. Toggling the MEG resulted in a different background phase which is visible for MEG amplitudes. The quantitative analysis using the RAE showed that the difference between repeated measurements with same MEG polarity (32 mT/m: $2.5 \pm 2.4\%$) is lower than with toggled MEG polarity (32 mT/m: $10.6 \pm 7.8\%$). The error decreased with decreasing MEG amplitude. The displacement encoded by the imaging gradients $m(u)$ was small compared to the displacement encoded by the larger MEGs, although this estimate depends on the applied vibration frequency and is likely higher for higher frequencies.

MEG amplitude in mT/m	Dynamic range in μm	Encoded displacement in rad	RAE_+ in %	RAE_- in %
32	7	3.59 (1.24)	2.5 (2.4)	10.6 (7.8)
24	9	2.75 (0.97)	2.4 (2.4)	7.8 (5.3)
16	13	1.87 (0.65)	2.1 (2.2)	6.0 (3.7)
8	26	0.98 (0.33)	2.2 (2.2)	3.7 (2.7)
4	52	0.55 (0.15)	2.1 (2.2)	2.8 (2.5)
2	104	0.36 (0.06)	2.0 (2.2)	2.5 (2.5)
Imaging gradients	149	0.27 (0.05)		

Table 2: Encoding efficiency and mean absolute encoded displacement as group averages for different MEG amplitudes and the imaging gradients. In addition, averaged relative absolute differences RAE for repeated measurements with same and opposite polarity are given. Standard deviations are given in brackets.

4.2 Dual and multiple encoding unwrapping

Figure 4 shows the different phase reconstructions of a single timestep for different MEG combinations with the same dynamic range of the MEG with 8 mT/m amplitude for one representative slice. In addition reconstructed elastograms of SWS are displayed. At the top, results are given for the original data, which is the phase encoded by the MEG only. Results with added noise are shown at the bottom. OMME with three MEGs (32, 16, 8 mT/m and 32, 24, 16 mT/m) was compared to dual encoding strategies using 32 and 24 mT/m, 24 and 16 mT/m, 16 and 8 mT/m, 32 and 8 mT/m. It is well visible that dual encoding with 32 and 24 mT/m performed worst in terms of reconstruction failures, which subsequently corrupted the reconstructed elastogram. Despite no apparent reconstruction failures in the selected slice, also the other approaches showed defects in the final elastograms, which resulted from reconstruction failures on other timesteps or components. Moreover encoding approaches using higher MEGs showed less noise in the reconstructed phase

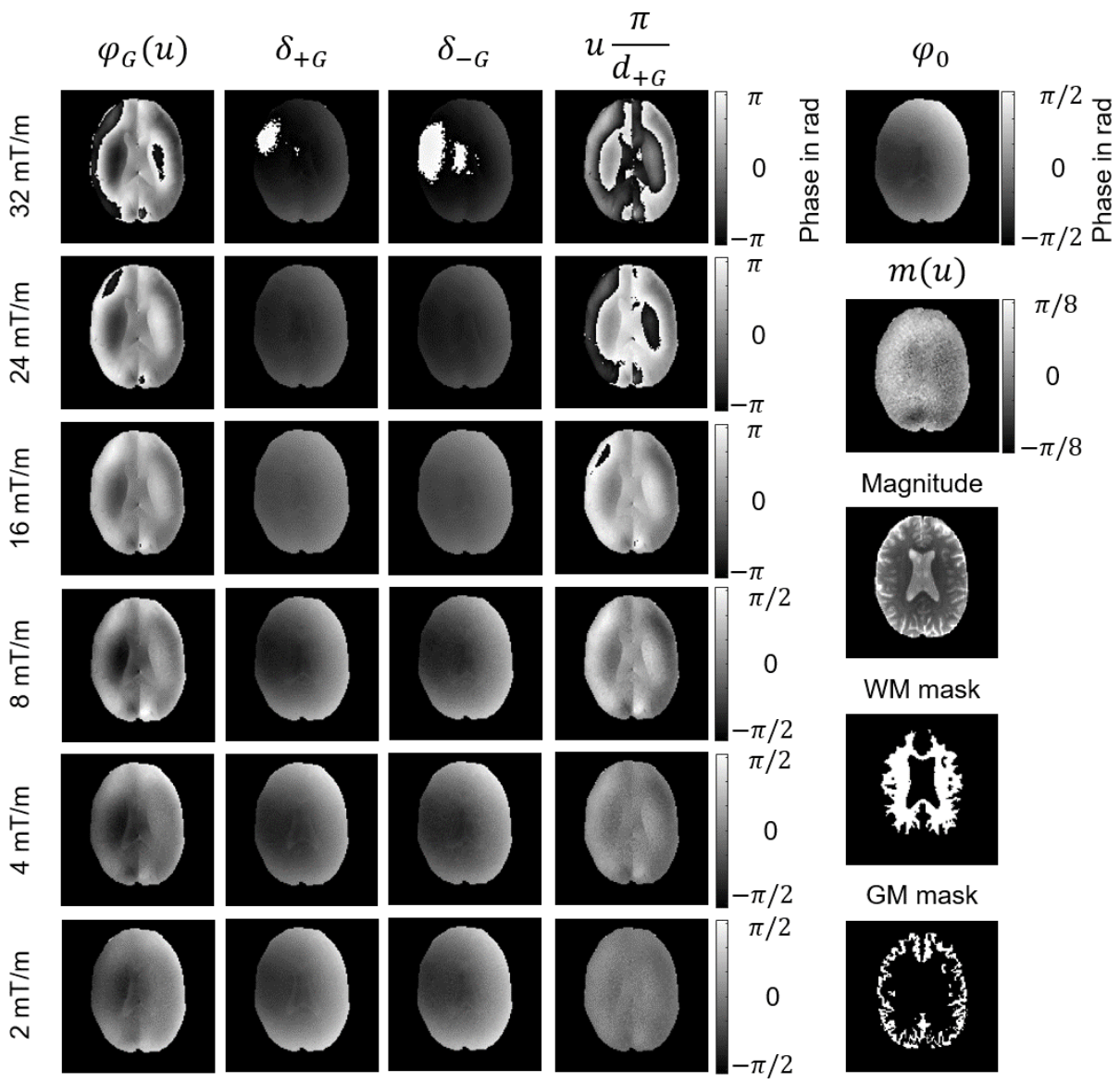

Figure 3: Measured phase $\varphi_G(u)$ of the complex MR signal in one representative slice, encoding direction (anterior-posterior) and subject for different MEG ampltiudes ranging from 32 mT/m to 2 mT/m. The separated phase contributions correspond to the model $\varphi_G(u) = \varphi_0 + \delta_G + m(u) + u\frac{\pi}{d_G}$ with $u\frac{\pi}{d_G}$ being the motion u encoded by the MEG with dynamic range d_G and the background phase due to the static phase of the imaging gradients φ_0, the static MEG-dependent phase δ_G and the motion-dependent phase encoded by the imaging gradients $m(u)$. Additionally the static-background phase δ_{-G} for toggled MEG polarity is shown. MRE mean magnitude image and masks for white matter (WM) and gray matter (GM) are given as reference. The color scale of the phase images was adapted at each figure for better visualization.

image. Adding noise to the complex data before reconstruction increased the number of reconstruction failures and noise of the combined image in all approaches. Consequently more corrupted voxels were visible in the final elastogram.

Table 3 summarizes the findings as relative error rates for the phase images (3a) and for the elastograms (3b) compared to the total amount of voxels (mean $\pm$ SD: $43,639 \pm 3,114$) inside the GM and WM mask for each subject. Incorporating all timesteps and encoding directions resulted in a total 1,047,336 voxel which could possibly fail to be reconstructed properly. In addition MNR of reconstructed phase images is tabled (3c). All numbers are given as group average and standard deviations in brackets.

In general, only little reconstruction failures ($< 1\%$) were observed in comparison to all possible voxels in the phase images. Only the dual encoding with 32 and 24 mT/m with 15% added noise showed failures above 4%. However, due to the combinatorial nature of SWS reconstruction which combines up to 24 phase images to one SWS image, the error rates became substantial for the elastograms. The relative differences between the reconstruction approaches were conserved. For the original data, dual encoding with 32 and 24 mT/m performed significantly worse ($3.9 \pm 3.4\%$) than OMME with 32, 16, 8 mT/m ($0.4 \pm 0.4\%, p = 0.001$). There was no statistical difference between the other encoding strategies ($p > 0.99$). Nonetheless the MNR scaled with the highest MEG amplitude used, such that approaches with 32 mT/m had a MNR of 17 ± 3 dB, 24 mT/m gave 15 ± 3 dB and 16 mT/m gave 12 ± 3 dB. Adding noise to the original data inflated error rates in all approaches which became larger than 40% for the noise sensitive dual encoding approach with 32 and 24 mT/m. With increased noise, OMME with 32, 16, 8 mT/m ($1.5 \pm 0.9\%$) also significantly outperformed the dual encoding with 24 and 16 mT/m ($6.9 \pm 1.3\%, p = 0.03$) and 32 and 8 mT/m ($16.8 \pm 7.7\%, p < 0.0001$) in terms of reduced reconstruction failures. These findings are supported in the theory section. OMME with 32, 24, 16 mT/m shows higher error rates in the elastograms with added noise ($2.6 \pm 1.4\%$) than the combination 32, 16, 8 mT/m, what is expected due to the poor performance of 32, 24 mT/m. Therefore, OMME with 32, 16, 8 mT/m is the most noise robust unwrapping approach tested here. Needless to say, that MNR was reduced when noise was added and MNR differences between the approaches were conserved. The last row of Table 3 indicates an increased MNR with additional postprocessing as described in Section 3.8. MNR improvements with respect to the original data were achieved in all cases. Figure 5 shows the corresponding elastograms in three volunteers for the comparison between the original data and the additional postprocessing. The increased MNR is again evident.

4.3 Comparison to other unwrapping methods

Figure 6 shows representative results for the SWS maps reconstructed from wrap-free phase images. The unwrapping was either performed using OMME utilizing phase images from MEG amplitude of 32, 16 and 8 mT/m or by Laplacian and Flynn unwrapping algorithms applied to the PC image of 32 mT/m MEG amplitude. Anatomical reference images are based on T2 weighted MRE magnitude images. Red arrows indicate areas where OMME based SWS reconstruction visually outperforms the other two approaches. Overall the noise outside the brain was largely reduced using OMME and tissue/air interfaces were sharper. Especially the transition between the skull and the brain tissue was properly reconstructed, while the unwrapping methods smoothed that region which lead to spurious stiffness values and reduced contrast.

In the first subject, it was especially difficult to demarcate the tissue/air boundary in the area of the left superior temporal sulcus using SWS reconstruction based on Laplacian and Flynn

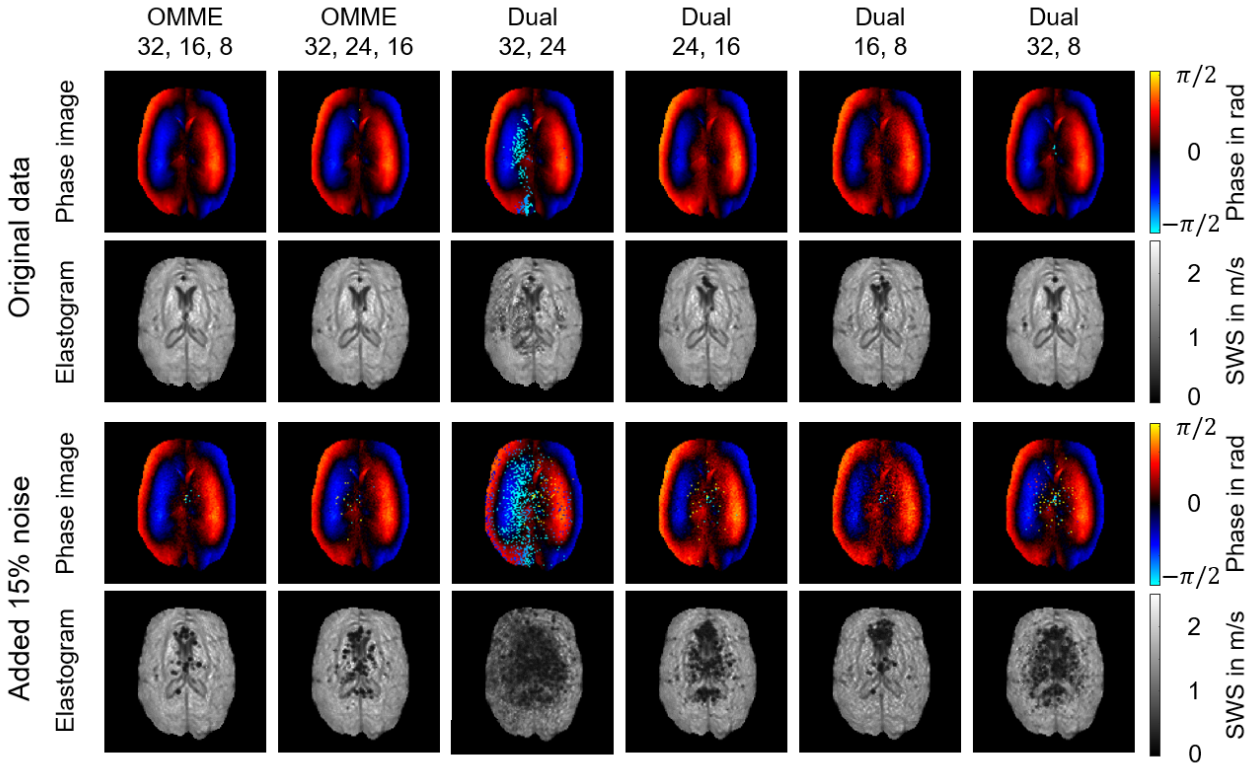

Figure 4: Different phase reconstructions of a single timestep with the same dynamic range d_{eff} using multiple motion encoding measurements. Here OMME with three MEGs (32, 16, 8 mT/m) and (32, 24, 16 mT/m) is compared to dual encoding using 32 and 24 mT/m, 24 and 16 mT/m, 16 and 8 mT/m, 32 and 8 mT/m. The bottom row shows the same reconstructions with added Gaussian noise with a standard deviation of 15% of the mean absolute encoded phase in WM.

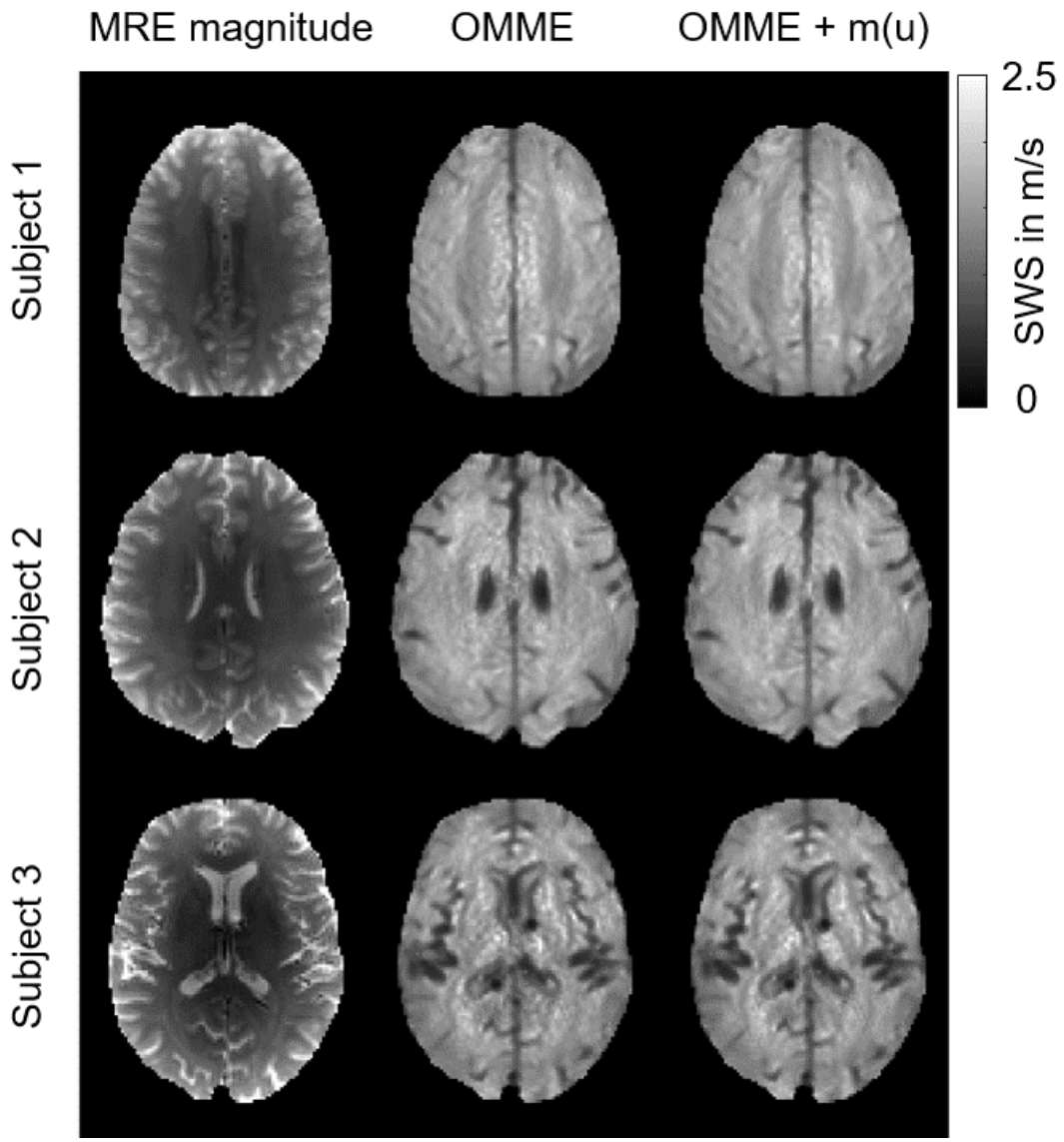

Figure 5: SWS maps based on wrap-free phase images using OMME (32, 16, 8 mT/m), without (mid column) and with (right column) applying Formula (23) for selected slices in three subjects. The anatomical reference image from T2 weighted MRE magnitude is included.

	OMME 32, 16, 8	OMME 32, 24, 16	Dual 32, 24	Dual 24, 16	Dual 16, 8	Dual 32, 8
Phase images						
Original data	0.06 (0.04)	0.07 (0.04)	0.26 (0.18)	0.07 (0.04)	0.06 (0.04)	0.09 (0.06)
+15% noise	0.2 (0.09)	0.33 (0.14)	4.11 (0.89)	0.79 (0.2)	0.2 (0.08)	1.73 (0.06)
Elastograms						
Original data	0.4 (0.4)	0.5 (0.4)	3.9 (3.4)	0.4 (0.3)	0.4 (0.4)	1.1 (1.0)
+15% noise	1.5 (0.9)	2.6 (1.4)	40.8 (9.9)	6.9 (1.3)	1.4 (0.5)	16.8 (7.7)
MNR						
Original data	17.2 (3)	17 (3)	17 (3)	15.1 (3.1)	12.4 (2.8)	17 (3)
+15% noise	9.8 (2.2)	9.7 (2.9)	10.1 (1.5)	9.1 (1.4)	5.1 (1.8)	7.8 (3.0)
+m(u)	18.8 (2.2)	18.5 (2.4)	18.6 (1.5)	16.8 (1.4)	13.7 (1.8)	18.3 (2.5)

Table 3: Number of wrongly reconstructed voxels in % in phase images and elastograms and MNR for OMME using three MEGs and different dual encoding strategies. Group mean values were averaged over WM and GM and tabled as group mean (sd). All combinations exhibit the same dynamic range d_G with different noise sensitivities to the input image noise σ_φ and different noise levels of the reconstructed phase images (MNR). In addition results with added Gaussian noise (15 % of the mean absolute encoded phase in WM) and added m(u) are given. MEG amplitudes are given in mT/m.

unwrapping. Only OMME allowed a good boundary detection. A similar effect was visible at the lingula gyrus where the space between the two hemispheres was only preserved properly with OMME. For subject two, the central part of the right lateral ventrical showed spurious SWS values for Laplacian and Flynn unwrapping probably due to tissue/fluid boundary artifacts which were enhanced by the algorithms. OMME based reconstruction showed higher level of details by fully recovering the boundaries between brain tissue and either ventricles or gyri. In the magnitude image of subject three susceptibility artifacts are present. However, OMME based SWS reconstruction showed a good agreement with the anatomical reference and correctly reconstructs SWS values associated with tissue voxels in the area of the temporal pole. In contrast, Laplacian based SWS maps are heavily corrupted and no reference to the anatomical image is present. Flynn performs better but still with noisy SWS values and blurred CSF/tissue (solid/fluid) boundaries. Similar observations are visible in a more cranial area of the temporal pole in subject four. Noisy SWS values make the demarcation of the temporal pole difficult for Laplacian and Flynn unwrapping SWS reconstructions.

The MNR analysis based on wrap-free phase images with a MEG amplitude of 32 mT/m revealed for Laplacian unwrapping a group mean MNR of 15.9 ± 2.7 dB and for Flynn unwrapping 15.6 ± 2.4 dB. Both results are significantly lower than the MNR for OMME based unwrapping as listed in table 3 ($p = 0.02$).

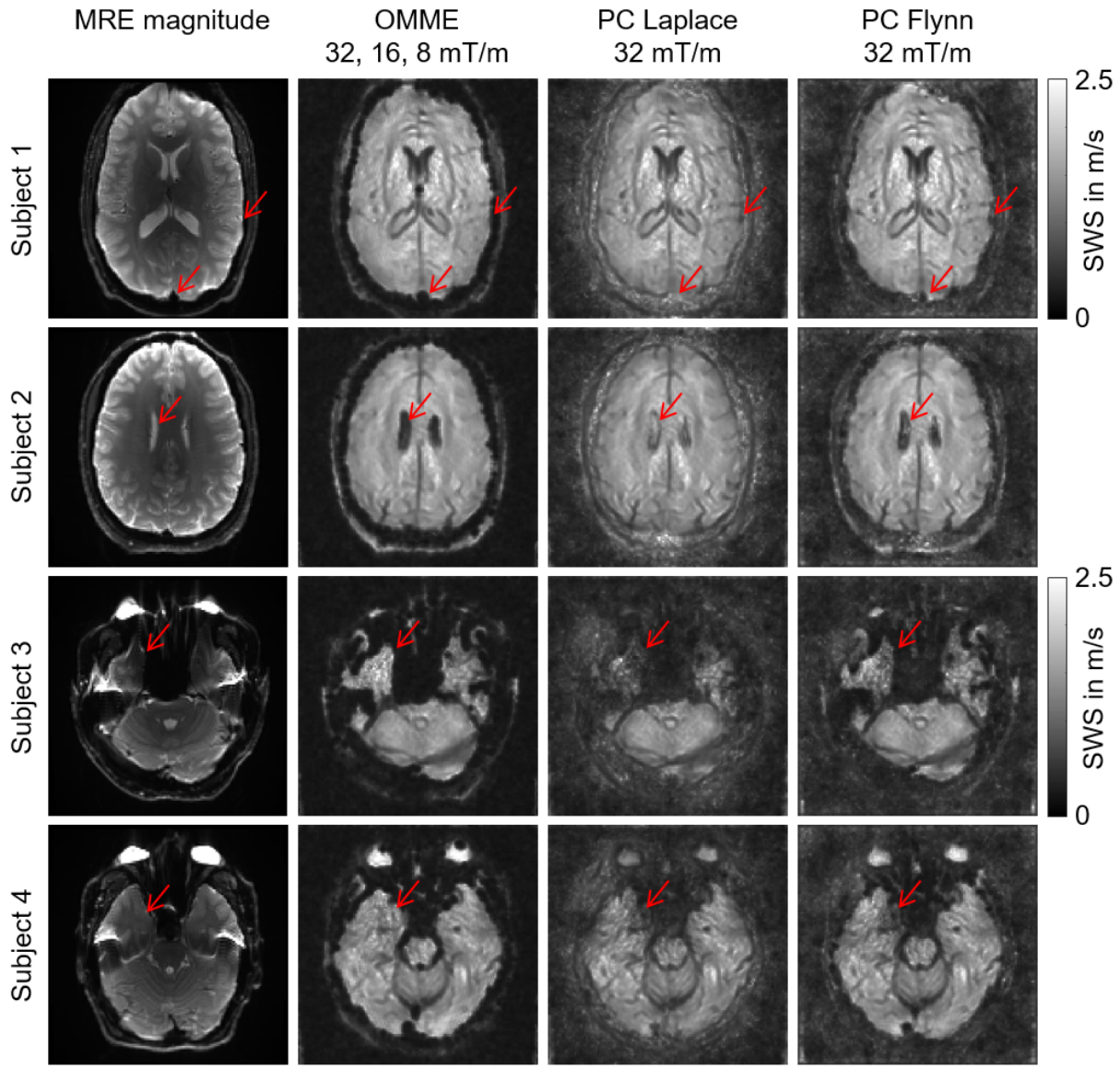

Figure 6: SWS maps based on wrap-free phase images using OMME (32, 16, 8 mT/m), Laplacian unwrapping and Flynn unwrapping for selected slices in four subjects. The anatomical reference image from T2 weighted MRE magnitude is included. Red arrows indicate areas where OMME shows more details and greater contrast in the SWS map.

5 Discussion

We have developed, theoretically analyzed and assessed in numerical and human brain data a new method for combining an arbitrary number of motion-encoded PC-MRI images, the Optimal Multiple Motion Encoding method (OMME).

We compared the proposed method with dual motion encoding strategies and common phase unwrapping algorithms in terms of unwrapping success, MNR and quality of subsequently reconstructed SWS maps. To the best of the author's knowledge, this is the first reported method for combining a larger number of motion encoded images obtained from different MEGs.

For a fixed effective dynamic range of the encoded motion, OMME presents a superior performance with respect to noise compared to standard dual encoding unwrapping. This was assessed analytically and confirmed numerically in a "single voxel" experiment. The analysis on the in vivo data with respect to reconstruction failures and MNR confirm these findings. Additionally it was shown that inverting the MEG polarity affects the induced background phase of the MEG which is not critical for our proposed method, but it should be considered in classical PC approaches where a phase-difference image is calculated to remove contaminant phase information.

It was shown that unwrapping is most robust to noise when N images are combined which were measured in the dynamic ranges $d_1, \ldots, d_N$ such that $d_i = 2^{-i+1} d_1$. This simplifies the acquisition protocol allowing the scanner operator to select the largest MEG and the number of measurements N only, as it is usually done when the MEG is kept fixed.

The OMME was compared against standard unwrapping methods (Laplacian and Flynn). Remarkably, OMME allows to improve the SWS maps by reducing the noise in the wave images without spatial smoothing as Laplace unwrapping does and without unwrapping failure as it may occur with Flynn unwrapping predominantly at boundaries. This showed that details can be preserved which are otherwise smoothed (out) by standard unwrapping methods. This can be relevant for higher resolution MRE in a variety of applications including tumor detection or characterization of lesion in multiple sclerosis (MS) [48]. Moreover, we showed that standard unwrapping methods smear boundaries between fluid filled spaces and brain tissue. This not only affects cortical areas of the brain and their tissue/air boundaries but also interfaces between tissue and fluid filled ventricles. The importance of proper reconstruction of stiffness estimates for cortical areas has recently been addresses by Lilay *et al.* [49]. If tissue mechanical properties are altered at those boundaries, e.g. as a result of impaired CSF-brain barriers in MS [50] OMME based wrap-free MRE phase images could be sensitive to those alterations. Also other interfaces between tumor and healthy tissue could potentially be better resolved. Further, the increased dynamic range of OMME with good MNR properties could be utilized when high frequency vibrations induce heavy wraps near the source and are quickly damped towards small deflection amplitudes inside the tissue under investigation. The potential of OMME for higher frequency MRE needs to be further investigated. Without heavy wraps, Laplacian and Flynn unwrapping methods performed similar, which underlines that OMME might be very suitable for high MNR applications.

The postprocessing introduced in Section 3.8 allows for an improvement in the SWS image quality at no additional scan time and at negligible computational cost. Since this assumes large MEG encoding efficiencies compared with those of the imaging gradients, the applicability should be investigated with respect to each specific scanning protocol.

As a limitation of OMME, examination times are increased by additional measurements for multiple MEGs. Each applied MEG increases the total scan time by the acquisition time of one measurement. Moreover, the background phase (i.e. MEGs on and vibration off) needs to be

measured, which still is required at one timestep only for all encoding directions, adding another 1/(number of timesteps) * acquisition time. Nevertheless, the time investment pays off when phase wraps can be avoided and maps are generated that are more detailed than standard methods. Even resolving wraps only partly supports unwrapping algorithms and permits higher encoding efficiencies than standard MRE towards measurement of damped waves without corrupting high amplitude regions. In addition, noise sources other than those mentioned could also affect OMME performance. For example, induced movements due to scanner table vibrations are encoded as a function of MEG amplitude and cannot be corrected. However, this was not a problem here because the wave amplitudes were probably strong enough.

OMME can be also applied to to other PC-MRI methods like e.g. flow MRI. In that case the dynamic range will be the *venc* parameter. However, some careful noise analysis may be needed when the then phase that does not depend on the motion is measured only once, as it is the case in 4D Flow, since then the phase differences for each *venc* will be correlated. This might be investigated in a future work.

6 Conclusion

In this study, we proposed an optimal multiple motion encoding (OMME) method which is suitable for motion sensitive PC-MRI. A detailed theoretical analysis was provided to derive a rationale for choosing the combinations of motion encoding gradients that lead to robust unwrapping for a given effective dynamic range when SNR in the phase images decreases. We applied novel OMME to MRE measurements of in vivo human brain acquisitions. It was shown that OMME outperforms dual encoding strategies and allows to recover more tissue details due to its increased MNR ratio within a high dynamic range leading to SWS maps which preserve important details such as discontinuities in the stiffness. Especially for applications of high resolution MRE wrap-free images with proper MNR – as provided by OMME – are desired.

As we showed in the theory section, OMME will fail in unwrapping to the given dynamic range when further increasing the noise in the phase images. Depending on the value of beta, images may be wrap-free or not, what is given by the relation between the effective dynamic range and beta.

Conflict of interest

The authors declare no conflict of interest.

Acknowledgments

H.H. and I.S. acknowledge the funding from the German Research Foundation (GRK 2260 BIOQIC, SFB1340 Matrix in Vision, Sa901/17-2) and from the European Union's Horizon 2020 Program (ID 668039, EU FORCE Imaging the Force of Cancer). C.B. acknowledges the funding from the European Research Council (ERC) under the European Union's Horizon 2020 research and innovation programme (grant agreement No 852544 - CardioZoom). AO was partially funded by ANID-Fondecyt 1191903, 1201311, CMM ACE210010 and FB210005 Basal-ANID funds, FONDAP/15110009, Millennium Programs $NCN17_1$, $NCN19_161$ and ACIPDE MATH190008, Climat-Amsud 21-Climat-05 projects. A.O and S.U. acknowledge funding from ANID Millennium Science Initiative Program – NCN17–129. H.C. acknowledges to Conicyt Basal Program AFB and 170001.

A Theoretical and practical aspects of OMME

A.1 Effective dynamic range

Here we prove that the effective dynamic range in OMME, corresponding to the smallest period of the cost function

$$J_N(u) = \sum_{j=1}^{N} \left(1 - \cos\left(\frac{\pi}{d_j}(u_j - u)\right)\right), \tag{24}$$

is the least common multiplier of $2d_1, \ldots, 2d_N$, i.e. $d_{eff} = d_1 a^{N-1}$, under the assumption that $d_j = (a/b)^{j-1} d_1$, with $a < b \in \mathbb{N}$.

We proceed as it is usual for these problems: find the smallest possible value $T > 0$ such that $J_N(u) = J_N(u+T)$, i.e.:

$$\begin{aligned}
\sum_{j=1}^{N} \cos\left(\frac{\pi}{d_j}(u_j - u)\right) &= \sum_{j=1}^{N} \cos\left(\frac{\pi}{d_j}(u_j - u + T)\right) \\
&= \sum_{j=1}^{N} \left[\cos\left(\frac{\pi}{d_j}(-u)\right)\cos\left(\frac{\pi}{d_j}(u_j + T)\right) - \sin\left(\frac{\pi}{d_j}(-u)\right)\sin\left(\frac{\pi}{d_j}(u_j + T)\right)\right] \\
&= \sum_{j=1}^{N} \left[\cos\left(\frac{\pi}{d_j}u\right)\cos\left(\frac{\pi}{d_j}(u_j + T)\right) + \sin\left(\frac{\pi}{d_j}u\right)\sin\left(\frac{\pi}{d_j}(u_j + T)\right)\right]. \qquad (25)
\end{aligned}$$

Due to the fact that

$$\cos\left(\frac{\pi}{d_j}(u_j - u)\right) = \cos\left(\frac{\pi}{d_j}u_j\right)\cos\left(\frac{\pi}{d_j}u\right) + \sin\left(\frac{\pi}{d_j}u_j\right)\sin\left(\frac{\pi}{d_j}u\right), \tag{26}$$

Equation (25) becomes

$$\begin{aligned}
&\sum_{j=1}^{N} \left[\cos\left(\frac{\pi}{d_j}u\right)\left(\cos\left(\frac{\pi}{d_j}(u_j + T)\right) - \cos\left(\frac{\pi}{d_j}u_j\right)\right)\right. \\
&\left. + \sin\left(\frac{\pi}{d_j}u\right)\left(\sin\left(\frac{\pi}{d_j}(u_j + T)\right) - \sin\left(\frac{\pi}{d_j}u_j\right)\right)\right] = 0.
\end{aligned}$$

Note now, that the functions $\cos(\pi u/d_j)$ and $\sin(\pi u/d_j)$ are linearly independent in $\mathbb{R}$ for all values of j. Indeed, using the change of variable $x = \pi u/d_1/a^{N-1}$ the problem reduces to show that the following functions are linearly independent:

$$\cos\left(x b^{j-1} a^{N-j}\right), \sin\left(x b^{j-1} a^{N-j}\right), j = 1, \ldots, N, \tag{27}$$

which is true since $a^{N-1} < a^{N-2}b < \cdots < b^{N-1}$. Therefore, we obtain that the following relations need to be satisfied:

$$\cos\left(\frac{\pi}{d_j}(u_j + T)\right) - \cos\left(\frac{\pi}{d_j}u_j\right) = 0\ ,\ \sin\left(\frac{\pi}{d_j}(u_j + T)\right) - \sin\left(\frac{\pi}{d_j}u_j\right) = 0 \tag{28}$$

or using complex variable

$$\exp i\frac{\pi}{d_j}(u_j+T)=\exp i\frac{\pi}{d_j}u_j. \tag{29}$$

This leads to $T=\{2k_jd_j\}_{\forall k_j}$. Since this has to hold for all $j=1,\dots,N$ simultaneously, it proves that the smallest period T is the least common multiplier of $2d_1,\dots,2d_N$. This lead to the period being $T=2d_1a^{N-1}$.

A.2 Noise analysis

In the optimal dual encoding method, the unwrapped displacement corresponds to the global minimum with smallest magnitude, which we will denote u_*. Therefore, due to the $2d_{eff}$-periodicity, wraps will occur when $d_{eff}\leq|u_{true}|$. Notice that in opposite than the standard dual encoding for $\beta\neq 1/2$ we do not need u_{pc} for unwrapping: both u_1 and u_2 can be aliased, still resulting in an unwrapped u_*.

In [35], no theoretical noise analysis was performed, which will be shown here. First, we need an expression u_*, which can be obtained from the fact that the global minimum is also a local minimum, i.e. $J'_{dual}(u_*)=0$. Indeed

$$J'_{dual}(u_*)=-\frac{\pi}{d_1}\sin\left(\frac{\pi}{d_1}(u_1-u_*)\right)-\frac{\pi}{d_2}\sin\left(\frac{\pi}{d_2}(u_2-u_*)\right) \tag{30}$$

$$=-\frac{\pi}{d_1}\sin\left(\frac{\pi}{d_1}(u_1+2k_1d_1-u_*)\right)-\frac{\pi}{d_2}\sin\left(\frac{\pi}{d_2}(u_2+2k_2d_2-u_*)\right) \tag{31}$$

for all $k_1,k_2\in\mathbb{Z}$. Notice that $u_*\approx u_1+2k_1d_1\approx u_2+2k_2d_2$ for some fixed k_1,k_2 in case of small measurement noise in the phase (and equal if no noise is present). Hence, we can approximate the sin-terms by its arguments leading to:

$$u_*\approx\left(d_1^{-2}+d_2^{-2}\right)^{-1}\left(u_1d_1^{-2}+u_2d_2^{-2}+2\left(k_1d_1^{-1}+k_2d_2^{-1}\right)\right). \tag{32}$$

Since assume all that measurements are statistically independent (and therefore u_1 and u_2), the variance of u_* has the form

$$\mathrm{Var}(u_*)=\left(d_1^{-2}+d_2^{-2}\right)^{-2}\left(\mathrm{Var}(u_1)d_1^{-4}+\mathrm{Var}(u_2)d_2^{-4}\right) \tag{33}$$

$$=\left(d_1^{-2}+d_2^{-2}\right)^{-2}\left(\alpha^2d_1^{-4}+\alpha^2\beta^2d_2^{-4}\right)=\frac{\mathrm{Var}(u_2)}{1+\beta^2}<\mathrm{Var}(u_2). \tag{34}$$

Thus, an improved estimate in terms of variance is obtained.

Analogously to the dual encoding case, the optimum can be found to approximately be

$$u_*\approx\left(\sum_{j=1}^N d_j^{-2}\right)^{-1}\left(\sum_{j=1}^N u_jd_j^{-2}+2k_jd_j^{-1}\right),\qquad k_j\in\mathbb{Z},\ j=1,\dots,N \tag{35}$$

with variance

$$\mathrm{Var}(u_*)=\left(\sum_{j=1}^N d_j^{-2}\right)^{-2}\sum_{j=1}^N\mathrm{Var}(u_j)d_j^{-4}=2\sigma_\varphi^2\left(\sum_{j=1}^N d_j^{-2}\right)^{-2}\sum_{j=1}^N d_j^{-2} \tag{36}$$

$$=2\sigma_\varphi^2\left(\sum_{j=1}^N d_j^{-2}\right)^{-1}=\mathrm{Var}(u_N)\left(\sum_{j=1}^N\left(\frac{d_N}{d_j}\right)^2\right)^{-1}<\mathrm{Var}(u_N) \tag{37}$$

If we consider the case $d_N = d_j \beta^{N-j}$ for $j = 1, \ldots, N$, we obtain:

$$\mathrm{Var}(u_*) = \mathrm{Var}(u_N)\beta^{-2N}\left(\sum_{j=1}^{N}\beta^{-2j}\right)^{-1} = \mathrm{Var}(u_N)\frac{1-\beta^2}{1-\beta^{2N}} = \mathrm{Var}(u_1)\beta^{2(N-1)}\frac{1-\beta^2}{1-\beta^{2N}}. \quad (38)$$

Note the exponential reduction of the standard deviation with respect to the number of measurements, instead of the linear reduction obtained by averaging equal dynamic range data (i.e. $\beta = 1$).

References

[1] Monvadi Srichai, Ruth Lim, Samson Wong, and Vivian Lee. Cardiovascular applications of phase-contrast mri. American Journal of Roentgenology, 192(3):662–675, 2009.

[2] Michael Markl, Alex Frydrychowicz, Sebastian Kozerke, Mike Hope, and Oliver Wieben. 4d flow mri. Journal of Magnetic Resonance Imaging, 36(5):1015–1036, 2012.

[3] Petter Dyverfeldt, Malenka Bissell, Alex J Barker, Ann F Bolger, Carl-Johan Carlhäll, Tino Ebbers, Christopher J Francios, Alex Frydrychowicz, Julia Geiger, Daniel Giese, Michael Hope, Philip Kilner, Sebastian Kozerke, Saul Myerson, Stefan Neubauer, Oliver Wieben, and Michael Markl. 4d flow cardiovascular magnetic resonance consensus statement. Journal of Cardiovascular Magnetic Resonance, 17:72, 2015.

[4] R Muthupillai, DJ Lomas, PJ Rossman, James F Greenleaf, Armando Manduca, and Richard Lorne Ehman. Magnetic resonance elastography by direct visualization of propagating acoustic strain waves. science, 269(5232):1854–1857, 1995.

[5] Yogesh K Mariappan, Kevin J Glaser, and Richard L Ehman. Magnetic resonance elastography: a review. Clinical anatomy, 23(5):497–511, 2010.

[6] Dieter Klatt, Uwe Hamhaber, Patrick Asbach, Jürgen Braun, and Ingolf Sack. Noninvasive assessment of the rheological behavior of human organs using multifrequency mr elastography: a study of brain and liver viscoelasticity. Physics in Medicine & Biology, 52(24):7281, 2007.

[7] Siddharth Singh, Sudhakar K Venkatesh, Zhen Wang, Frank H Miller, Utaroh Motosugi, Russell N Low, Tarek Hassanein, Patrick Asbach, Edmund M Godfrey, Meng Yin, et al. Diagnostic performance of magnetic resonance elastography in staging liver fibrosis: a systematic review and meta-analysis of individual participant data. Clinical Gastroenterology and Hepatology, 13(3):440–451, 2015.

[8] Kay M Pepin, Richard L Ehman, and Kiaran P McGee. Magnetic resonance elastography (mre) in cancer: technique, analysis, and applications. Progress in nuclear magnetic resonance spectroscopy, 90:32–48, 2015.

[9] Huiming Dong, Richard D White, and Arunark Kolipaka. Advances and future direction of magnetic resonance elastography. Topics in magnetic resonance imaging: TMRI, 27(5):363, 2018.

[10] Armando Manduca, Philip J Bayly, Richard L Ehman, Arunark Kolipaka, Thomas J Royston, Ingolf Sack, Ralph Sinkus, and Bernard E Van Beers. Mr elastography: Principles, guidelines, and terminology. Magnetic Resonance in Medicine, 85(5):2377–2390, 2021.

[11] Meng Yin, John Woollard, Xiaofang Wang, Vicente E Torres, Peter C Harris, Christopher J Ward, Kevin J Glaser, Armando Manduca, and Richard L Ehman. Quantitative assessment of hepatic fibrosis in an animal model with magnetic resonance elastography. Magnetic Resonance in Medicine: An Official Journal of the International Society for Magnetic Resonance in Medicine, 58(2):346–353, 2007.

[12] Gergely Bertalan, Charlotte Klein, Stefanie Schreyer, Barbara Steiner, Bernhard Kreft, Heiko Tzschätzsch, Angela Ariza de Schellenberger, Melina Nieminen-Kelhä, Jürgen Braun, Jing Guo, et al. Biomechanical properties of the hypoxic and dying brain quantified by magnetic resonance elastography. Acta Biomaterialia, 101:395–402, 2020.

[13] Jing Guo, Gergely Bertalan, David Meierhofer, Charlotte Klein, Stefanie Schreyer, Barbara Steiner, Shuangqing Wang, Rafaela Vieira da Silva, Carmen Infante-Duarte, Stefan Koch, et al. Brain maturation is associated with increasing tissue stiffness and decreasing tissue fluidity. Acta Biomaterialia, 99:433–442, 2019.

[14] Thomas Elgeti, Michael Laule, Nikola Kaufels, Jörg Schnorr, Bernd Hamm, Abbas Samani, Jürgen Braun, and Ingolf Sack. Cardiac mr elastography: comparison with left ventricular pressure measurement. Journal of cardiovascular magnetic resonance, 11(1):1–10, 2009.

[15] Ingolf Sack, Jens Rump, Thomas Elgeti, Abbas Samani, and Jürgen Braun. Mr elastography of the human heart: noninvasive assessment of myocardial elasticity changes by shear wave amplitude variations. Magnetic Resonance in Medicine: An Official Journal of the International Society for Magnetic Resonance in Medicine, 61(3):668–677, 2009.

[16] Sebastian Papazoglou, Jürgen Braun, Uwe Hamhaber, and Ingolf Sack. Two-dimensional waveform analysis in mr elastography of skeletal muscles. Physics in Medicine & Biology, 50(6):1313, 2005.

[17] Felix Schrank, Carsten Warmuth, Steffen Görner, Tom Meyer, Heiko Tzschätzsch, Jing Guo, Yavuz Oguz Uca, Thomas Elgeti, Jürgen Braun, and Ingolf Sack. Real-time mr elastography for viscoelasticity quantification in skeletal muscle during dynamic exercises. Magnetic Resonance in Medicine, 84(1):103–114, 2020.

[18] Patrick Asbach, Dieter Klatt, Uwe Hamhaber, Jürgen Braun, Rajan Somasundaram, Bernd Hamm, and Ingolf Sack. Assessment of liver viscoelasticity using multifrequency mr elastography. Magnetic Resonance in Medicine: An Official Journal of the International Society for Magnetic Resonance in Medicine, 60(2):373–379, 2008.

[19] Sudhakar Kundapur Venkatesh and Richard L Ehman. Magnetic resonance elastography of abdomen. Abdominal imaging, 40(4):745–759, 2015.

[20] Florian Dittmann, Heiko Tzschätzsch, Sebastian Hirsch, Eric Barnhill, Jürgen Braun, Ingolf Sack, and Jing Guo. Tomoelastography of the abdomen: tissue mechanical properties of the liver, spleen, kidney, and pancreas from single mr elastography scans at different hydration states. Magnetic resonance in medicine, 78(3):976–983, 2017.

[21] Sudhakar K Venkatesh, Meng Yin, and Richard L Ehman. Magnetic resonance elastography of liver: technique, analysis, and clinical applications. Journal of magnetic resonance imaging, 37(3):544–555, 2013.

[22] Ingolf Sack, Bernd Beierbach, Jens Wuerfel, Dieter Klatt, Uwe Hamhaber, Sebastian Papazoglou, Peter Martus, and Jürgen Braun. The impact of aging and gender on brain viscoelasticity. Neuroimage, 46(3):652–657, 2009.

[23] Arvin Arani, Matthew C Murphy, Kevin J Glaser, Armando Manduca, David S Lake, Scott A Kruse, Clifford R Jack Jr, Richard L Ehman, and John Huston 3rd. Measuring the effects of aging and sex on regional brain stiffness with mr elastography in healthy older adults. Neuroimage, 111:59–64, 2015.

[24] Patricia S Lan, Kevin J Glaser, Richard L Ehman, and Gary H Glover. Imaging brain function with simultaneous bold and viscoelasticity contrast: fmri/fmre. NeuroImage, 211:116592, 2020.

[25] Lucy V Hiscox, Curtis L Johnson, Matthew DJ McGarry, Hillary Schwarb, Edwin JR van Beek, Neil Roberts, and John M Starr. Hippocampal viscoelasticity and episodic memory performance in healthy older adults examined with magnetic resonance elastography. Brain imaging and behavior, 14(1):175–185, 2020.

[26] Joshua D Hughes, Nikoo Fattahi, Jamie Van Gompel, Arvin Arani, Fredric Meyer, Giuseppe Lanzino, Michael J Link, Richard Ehman, and John Huston. Higher-resolution magnetic resonance elastography in meningiomas to determine intratumoral consistency. Neurosurgery, 77(4):653–659, 2015.

[27] John Huston III, Matthew C Murphy, Bradley F Boeve, Nikoo Fattahi, Arvin Arani, Kevin J Glaser, Armando Manduca, David T Jones, and Richard L Ehman. Magnetic resonance elastography of frontotemporal dementia. Journal of Magnetic Resonance Imaging, 43(2):474–478, 2016.

[28] Eric Barnhill, Paul Kennedy, Curtis L Johnson, Marius Mada, and Neil Roberts. Real-time 4d phase unwrapping applied to magnetic resonance elastography. Magnetic resonance in medicine, 73(6):2321–2331, 2015.

[29] Michael Loecher, Eric Schrauben, Kevin Johnson, and Oliver Wieben. Phase unwrapping in 4d mr flow with a 4d single-step laplacian algorithm. Journal of Magnetic Resonance Imaging, 43(4):833–842, 2016.

[30] Thomas J Flynn. Two-dimensional phase unwrapping with minimum weighted discontinuity. JOSA A, 14(10):2692–2701, 1997.

[31] Ingolf Sack, Jens Rump, Thomas Elgeti, Abbas Samani, and Jurgen Braun. Mr elastography of the human heart: Noninvasive assessment of myocardial elasticity changes by shear wave amplitude variations. Magnetic Resonance in Medicine, 61(3):668–677, 2008.

[32] Marvin A Schofield and Yimei Zhu. Fast phase unwrapping algorithm for interferometric applications. Optics letters, 28(14):1194–1196, 2003.

[33] Adrian Lee, Bruce Pike, and Norbert Pelc. Three-point phase-contrast velocity measurements with increased velocity-to-noise ratio. Magnetic Resonance in Medicine, 33:122–128, 1995.

[34] Susanne Schnell, Sameer Ansari, Can Wu, Julio Garcia, Ian Murphy, Ozair Rahman, Amir Rahsepar, Maria Aristova, Jeremy Collins, James Carr, and Michael Markl. Accelerated dual-venc 4d flow mri for neurovascular applications. Journal of Magnetic Resonance Imaging, 46:102–114, 2017.

[35] H. Carrillo, A. Osses, S. Uribe, and C. Bertoglio. Optimal dual-venc (odv) unwrapping in phase-contrast mri. IEEE Transactions on Medical Imaging, 38:1263–1270, 2019.

[36] Ziying Yin, Yi Sui, Joshua D Trzasko, Phillip J Rossman, Armando Manduca, Richard L Ehman, and John Huston III. In vivo characterization of 3d skull and brain motion during dynamic head vibration using magnetic resonance elastography. Magnetic resonance in medicine, 80(6):2573–2585, 2018.

[37] Felix Schrank, Carsten Warmuth, Heiko Tzschätzsch, Bernhard Kreft, Sebastian Hirsch, Jürgen Braun, Thomas Elgeti, and Ingolf Sack. Cardiac-gated steady-state multifrequency magnetic resonance elastography of the brain: Effect of cerebral arterial pulsation on brain viscoelasticity. Journal of Cerebral Blood Flow & Metabolism, 40(5):991–1001, 2020.

[38] Mark A Griswold, Peter M Jakob, Robin M Heidemann, Mathias Nittka, Vladimir Jellus, Jianmin Wang, Berthold Kiefer, and Axel Haase. Generalized autocalibrating partially parallel acquisitions (grappa). Magnetic Resonance in Medicine: An Official Journal of the International Society for Magnetic Resonance in Medicine, 47(6):1202–1210, 2002.

[39] William D Penny, Karl J Friston, John T Ashburner, Stefan J Kiebel, and Thomas E Nichols. Statistical parametric mapping: the analysis of functional brain images. Elsevier, 2011.

[40] Sebastian Hirsch, Ingolf Sack, and Jurgen Braun. Magnetic resonance elastography: physical background and medical applications. John Wiley & Sons, 2017.

[41] Joaquin Mura, Felix Schrank, and Ingolf Sack. An analytical solution to the dispersion-by-inversion problem in magnetic resonance elastography. Magnetic Resonance in Medicine, 84(1):61–71, 2020.

[42] Heiko Tzschätzsch, Jing Guo, Florian Dittmann, Sebastian Hirsch, Eric Barnhill, Korinna Jöhrens, Jürgen Braun, and Ingolf Sack. Tomoelastography by multifrequency wave number recovery from time-harmonic propagating shear waves. Medical image analysis, 30:1–10, 2016.

[43] Helge Herthum, Sergio CH Dempsey, Abbas Samani, Felix Schrank, Mehrgan Shahryari, Carsten Warmuth, Heiko Tzschätzsch, Jürgen Braun, and Ingolf Sack. Superviscous properties of the in vivo brain at large scales. Acta biomaterialia, 121:393–404, 2021.

[44] David L Donoho, Iain M Johnstone, Gérard Kerkyacharian, and Dominique Picard. Wavelet shrinkage: asymptopia? Journal of the Royal Statistical Society: Series B (Methodological), 57(2):301–337, 1995.

[45] Gergely Bertalan, Jing Guo, Heiko Tzschätzsch, Charlotte Klein, Eric Barnhill, Ingolf Sack, and Jürgen Braun. Fast tomoelastography of the mouse brain by multifrequency single-shot mr elastography. Magnetic resonance in medicine, 81(4):2676–2687, 2019.

[46] Eric Barnhill, Lyam Hollis, Ingolf Sack, Jürgen Braun, Peter R Hoskins, Pankaj Pankaj, Colin Brown, Edwin JR van Beek, and Neil Roberts. Nonlinear multiscale regularisation in mr elastography: Towards fine feature mapping. Medical image analysis, 35:133–145, 2017.

[47] Ivan W Selesnick, Richard G Baraniuk, and Nick C Kingsbury. The dual-tree complex wavelet transform. IEEE signal processing magazine, 22(6):123–151, 2005.

[48] Kaspar-Josche Streitberger, Ingolf Sack, Dagmar Krefting, Caspar Pfüller, Jürgen Braun, Friedemann Paul, and Jens Wuerfel. Brain viscoelasticity alteration in chronic-progressive multiple sclerosis. PloS one, 7(1):e29888, 2012.

[49] Ledia Lilaj, Helge Herthum, Tom Meyer, Mehrgan Shahryari, Gergely Bertalan, Alfonso Caiazzo, Juergen Braun, Thomas Fischer, Sebastian Hirsch, and Ingolf Sack. Inversion-recovery mr elastography of the human brain for improved stiffness quantification near fluid solidboundaries. Magnetic Resonance in Medicine, n/a(n/a), 2021.

[50] Tsuneyuki Takeoka, Yukito Shinohara, Koichi Furumi, and Kosuke Mori. Impairment of blood-cerebrospinal fluid barrier in multiple sclerosis. Journal of Neurochemistry, 41(4):1102–1108, 1983.